Generalized quasilinear approximations in homogeneous shear turbulence

Zhenghao Luo, Carlos G. Hernández,[*] and Yongyun Hwang ⦿
Department of Aeronautics, Imperial College London,
South Kensington, London SW7 2AZ, United Kingdom

A generalized quasilinear (GQL) approximation [Marston *et al.*, Phys. Rev. Lett. **116**, 214501 (2016)] is applied to homogeneous shear turbulence following previous work on the quasilinear (QL) model [Hernández and Hwang, J. Fluid Mech. **904**, A11 (2020)]. For the GQL approximation, the velocity fluctuations are decomposed into low- and high-wave-number groups, the former of which is solved by considering the full nonlinear equations whereas the latter is obtained from the linearized equations around the former. Unlike the QL model, which typically shows significant inhibition of the energy cascade in the direction along which the linearization is made, the GQL model shows an energy cascade that is more active than the QL model because more Fourier modes included in the low-wave-number group allow for an extra energy transfer mechanism from the low- to high-wave-number group via the so-called "scattering" mechanism. It is shown that this scattering mechanism is most active when a relatively small and suitable number of Fourier modes are included in the low-wave-number group instead of a large number of the Fourier modes being so, and this is explained in terms of the neutral Lyapunov vector forming the solution to the linear equations for the high-wave-number group. As a consequence, the turbulence statics from the GQL model with a relatively small number of the Fourier modes in the low-wave-number group are closer to those from DNS than those from the model with a large number of the Fourier modes in the low-wave-number group. Finally, the QL/GQL approximations made in the streamwise and spanwise directions are compared, with emphasis on the role of slow pressure and the related pressure strain transport.

I. INTRODUCTION

Turbulent flows often exhibit a highly chaotic and multiscale behavior. The cost of resolving all scales involved down to the dissipation of energy (Kolmogorov scale) via direct numerical simulations (DNS) is often prohibitively expensive, especially for high Reynolds numbers. Therefore, there has been an increasing demand for reliable and accurate low-dimensional models which can provide a statistical description of turbulence as well as its main dynamical features at lower cost. Perhaps one of the earliest attempts was based on the utilization of the Navier-Stokes equations linearized around the time-averaged velocity to describe the coherent motions typically appearing in turbulent flows. A well-known example is the rapid distortion theory [1,2], where the linearized Navier-Stokes equations are used to predict the evolution of turbulent statistics in a rapidly

————————
[*]c.gonzalez-hernandez16@imperial.ac.uk

changing flow environment (e.g., high mean shear rate). In the last few decades, there have been a large number of studies which aimed to understand the origin of coherent structures in more general wall-bounded turbulent flows (e.g., Couette, pipe, channel, and boundary layer flows), where the mean flow is known to be linearly stable at typical transitional Reynolds numbers. In this type of flow, the evolution of disturbances has been studied by examining the response of the linearized Navier-Stokes equations to various excitations such as initial condition and harmonic and stochastic forcing [3–9], tools initially used for laminar flows at transitional Reynolds numbers. Additional studies have shown that these techniques could also be suitably refined to explain the emergence of energy-containing motions in turbulent flows (e.g., [5,10–15]).

Despite the recent advances made by these studies, the Navier-Stokes equations linearized about the stable mean flow alone are not able to describe sustaining turbulent velocity fluctuations. In this respect, the recently proposed quasilinear (QL)-type modeling offers an attractive direction to pursue, as it incorporates the nonlinearity of the equations in a minimal manner. A common theoretical basis of the QL approximation is the decomposition of the given flow into two groups: one in which all nonlinear terms are kept, and the other in which all self-interactions are either ignored or suitably modeled. The resulting equations for the first group are unchanged from the original, while those for the second become equivalent to a linearization around the first group sometimes with an additional (*ad hoc*) model (e.g., stochastic forcing, eddy viscosity, etc.). The earliest work utilizing the QL framework can be found in [16–18], where the self-interactions in the second group are simply ignored with application of the "marginal stability" closure (i.e., imposition of zero growth rate of the leading eigenmode to have a stationary solution). Modern variants employ more flexible approaches in the flow decomposition as well as in modeling of the self-interaction term in the second group: for example, stochastic structural stability theory (S3T) [19,20], direct statistical simulation (DSS) [21,22], self-consistent approximations [23,24], restricted nonlinear (RNL) model [25–32], generalized quasilinear approximations [33–36], and minimal quasilinear approximation augmented with eddy viscosity [37,38]. Finally, [39] recently performed a multiple-scale analysis of an archetypal slow-fast QL system.

The RNL approach, which we will refer to as the QL model hereafter, is the signpost of the present study, and it employs a decomposition of the given velocity into a streamwise mean and the fluctuation. Like a typical QL approximation, the former group is solved by the full nonlinear equations, whereas the latter is approximated with the linearized equations about the former. Without any extra modeling effort for the self-interacting nonlinear term in the second group, this model has been shown to successfully produce a reduced-order description of turbulence in wall-bounded shear flows at low Reynolds numbers [26–31]. This model was mathematically conceived to capture the key dynamics of coherent structures described by the so-called self-sustaining process [40,41], namely, the two-way interaction between a "streamwise elongated" structure of streamwise velocity (streaks) and streamwise wavy structures of cross-streamwise velocities (waves and rolls). In the QL model, the time-dependent dynamics of the streamwise-elongated streaks are well captured by the first group (i.e., streamwise mean), while the streamwise wavy structures are approximated by the equations linearized about the first.

In a previous work, Ref. [32] examined the spectral energy transfer of the QL model in uniform shear turbulence in the streamwise wave-number space. This choice of shear flow was particularly convenient since uniform shear turbulence has only a single integral length scale, and it also has self-sustaining process similar to the one in wall-bounded turbulence [42,43]. Therefore, the uniform shear turbulence enables us to study the effect of QL approximation on the self-sustaining process supported at a single integral scale and its energy cascade. The QL model was previously found to retain an active energy cascade in the spanwise wave-number space, whereas it significantly inhibited the energy cascade in the streamwise wave-number space due to the nature of the given approximation. It also results in highly elevated spectral energy intensity residing only at the integral streamwise length scale like in previous studies [25,29,30]. Importantly, Ref. [32] showed that the QL model is not able to incorporate some important role played by the slow pressure in distributing

the energy produced at the streamwise component to the wall-normal and spanwise components, resulting in the anisotropy of the fluid motions across all length scales including the Kolmogorov scale.

It becomes evident from [32] that the primary limitation of the QL model originates from the lack of the energy cascade in the streamwise direction due to the employed linearization for the second group of the velocity field. In the present study, we shall therefore take one step forward from the QL model by considering more of the energy cascade dynamics. To this end, the generalized quasilinear (GQL) approximation is applied here to uniform shear turbulence. The GQL approximation was originally proposed by [33,34,44–48] in the context of geophysical and astrophysical fluid dynamics to develop low-dimensional models based on the evolution of suitable statistical states (e.g., cumulants). More recently, it has also been used as a tool to study the nonlinear interactions in turbulent channel flow [35,36]. The GQL approximation typically decomposes the flow into two groups through a spectral cutoff filter: i.e., large and small scales. The former large-scale group is solved by considering the full nonlinear equations, while the latter small-scale group is obtained from the linearized equations around the former. In the limit of one streamwise (i.e., zero wave number) and all spanwise Fourier modes in the first group, the GQL approximation is reduced to the QL approximation [32]. On the other hand, if the first group includes all Fourier modes in both the streamwise and spanwise directions, it then becomes a DNS. In the present study, we will examine the energy transfer of the GQL approximation in both streamwise and spanwise wave-number space while evaluating its capability and accuracy at the same time.

The paper is organized as follows. The GQL model is introduced in Sec. II, where its spectral energy budget is formulated in Sec. II C and the numerical settings for simulations are provided in Sec. II D. In Sec. III the statistics and spectra of the GQL model are compared to those of DNS. The energy-budget and pressure-strain spectra are also presented here with a detailed analysis to explain the statistical features of the GQL model. Finally, the results are discussed in Sec. IV, and the paper concludes in Sec. V with some remarks.

II. FORMULATION

A. The generalized quasilinear approximation

We consider a turbulent flow under a uniform mean shear, in which the density and kinematic viscosity of the fluid are given by ρ and ν, respectively. The time is denoted by t, and the space is denoted by $\mathbf{x} = (x, y, z)$, with x, y, and z being the streamwise, vertical, and spanwise directions, respectively. For the GQL approximation, the velocity $\mathbf{u}$ is decomposed into two groups using a discrete Fourier transform in the streamwise and spanwise directions:

$$\mathbf{u} = \mathbf{U}_l + \mathbf{u}_h, \tag{1a}$$

where

$$\mathbf{U}_l(x, y, z) = \sum_{n=-M_{z,F}}^{M_{z,F}} \sum_{m=-M_{x,F}}^{M_{x,F}} \hat{\mathbf{u}}_{m,n}(y) e^{i(mk_{x,0}x + nk_{z,0}z)} \tag{1b}$$

and $\mathbf{u}_h = \mathbf{u} - \mathbf{U}_l$. Here $\hat{\mathbf{u}}_{m,n}$ is the discrete Fourier mode of the velocity, $k_{x,0}$ and $k_{z,0}$ are the fundamental streamwise and spanwise wave numbers defined by the horizontal computational domain (see Sec. II D for further details), and $M_{x,F}$ and $M_{z,F}$ in (1b) define the threshold streamwise and spanwise wave numbers in the decomposition such that $k_{x,c} = M_{x,F} k_{x,0}$ and $k_{z,c} = M_{z,F} k_{z,0}$.

Following the decomposition in (1), the projection operators $\mathcal{P}_l[\cdot]$ and $\mathcal{P}_h[\cdot]$ are defined such that

$$\mathcal{P}_l[\mathbf{u}] \equiv \mathbf{U}_l, \quad \mathcal{P}_h[\mathbf{u}] \equiv \mathbf{u}_h. \tag{2}$$

By the definition, they satisfy the following properties:

$$\mathcal{P}_l[\cdot] + \mathcal{P}_h[\cdot] = \mathcal{I}[\cdot], \tag{3a}$$

$$\mathcal{P}_l[\mathcal{P}_l[\cdot]] = \mathcal{P}_l[\cdot], \quad \mathcal{P}_h[\mathcal{P}_h[\cdot]] = \mathcal{P}_h[\cdot], \tag{3b}$$

$$\mathcal{P}_l[\mathcal{P}_h[\cdot]] = \mathcal{P}_h[\mathcal{P}_l[\cdot]] = \mathbf{0}, \tag{3c}$$

where $\mathcal{I}[\cdot]$ is the identity operator. These projection operators were first introduced in [49].

Using the definition (2) and the properties listed in (3), the Navier-Stokes equations are projected onto the $\mathcal{P}_l$ (or low wave number) and $\mathcal{P}_h$ (or high wave number) subspaces. The linearization of the equations for $\mathbf{u}_h$ about $\mathbf{U}_l$ leads to the GQL system of interest in the present study,

$$\frac{\partial \mathbf{U}_l}{\partial t} + \mathcal{P}_l[(\mathbf{U}_l \cdot \boldsymbol{\nabla})\mathbf{U}_l] = -\frac{1}{\rho}\boldsymbol{\nabla}P_l + \nu\nabla^2\mathbf{U}_l - \mathcal{P}_l[(\mathbf{u}_h \cdot \boldsymbol{\nabla})\mathbf{u}_h] \tag{4a}$$

and

$$\frac{\partial \mathbf{u}_h}{\partial t} + \mathcal{P}_h[(\mathbf{u}_h \cdot \boldsymbol{\nabla})\mathbf{U}_l] + \mathcal{P}_h[(\mathbf{U}_l \cdot \boldsymbol{\nabla})\mathbf{u}_h] = -\frac{1}{\rho}\boldsymbol{\nabla}p_h + \nu\nabla^2\mathbf{u}_h, \tag{4b}$$

where the pressures in the $\mathcal{P}_l$ and $\mathcal{P}_h$ subspaces, P_l and p_h, are defined to enforce $\boldsymbol{\nabla} \cdot \mathbf{U}_l = 0$ and $\boldsymbol{\nabla} \cdot \mathbf{u}_h = 0$, respectively, with $p = P_l + p_h$. Here the terms $\mathcal{P}_l[(\mathbf{U}_l \cdot \boldsymbol{\nabla})\mathbf{u}_h]$ and $\mathcal{P}_l[(\mathbf{u}_h \cdot \boldsymbol{\nabla})\mathbf{U}_l]$ are neglected in (4a), so that the energy averaged over the entire flow domain is conserved, following [33]. We note that the GQL approximation employed here reduces to the QL approximation if $M_{x,F} = 0$ and $M_{z,F} = N_{z,F}$, where $N_{z,F}$ is the total number of spanwise Fourier modes used for simulation. On the other hand, if $M_{x,F} = N_{x,F}$ and $M_{z,F} = N_{z,F}$ (with $N_{x,F}$ being the total number of streamwise Fourier modes used for simulation), then Eq. (4a) becomes identical to those used for DNS in the present work.

B. Reynolds decomposition

To analyze the turbulence statistics of the GQL and the original full equations of motion, we consider the Reynolds decomposition of the velocity $\mathbf{u} = (u, v, w)$:

$$\mathbf{u} = \mathbf{U} + \mathbf{u}', \tag{5}$$

where $\mathbf{U}(\equiv \langle\mathbf{u}\rangle_{x,z,t}) = (U(y), 0, 0)$ is the mean velocity with $\langle\cdot\rangle_{x,z,t}$ being an average in t-, x and z directions. The equation for the mean velocity is given by

$$\nu\frac{dU}{dy} - \langle u'v'\rangle_{x,z,t} = \frac{\tau_0}{\rho}, \tag{6a}$$

where the total applied shear stress is τ_0 and the Reynolds shear stress per unit density is $\langle u'v'\rangle_{x,z,t}$. The equations for the turbulent velocity fluctuation are then given by

$$\frac{\partial \mathbf{u}'}{\partial t} + (\mathbf{U} \cdot \boldsymbol{\nabla})\mathbf{u}' + (\mathbf{u}' \cdot \boldsymbol{\nabla})\mathbf{U} = -\frac{1}{\rho}\boldsymbol{\nabla}p' + \nu\nabla^2\mathbf{u}' - (\mathbf{u}' \cdot \boldsymbol{\nabla})\mathbf{u}'. \tag{6b}$$

We note that the Reynolds shear-stress term in (6a) does not appear in (6b) because it is spatially uniform in homogeneous shear turbulence.

For the GQL approximation to (6b), $\mathbf{u}'$ is further decomposed into low- and high-wave-number components:

$$\mathbf{u}' = \mathbf{u}_l + \mathbf{u}_h. \tag{7}$$

Using in (1) and (3), the projection of the equations for turbulent fluctuation onto the $\mathcal{P}_l$ and $\mathcal{P}_h$ subspaces leads to the following momentum equations:

$$\frac{\partial \mathbf{u}_l}{\partial t} + (\mathbf{u}_l \cdot \boldsymbol{\nabla})\mathbf{U} + (\mathbf{U} \cdot \boldsymbol{\nabla})\mathbf{u}_l = -\frac{1}{\rho}\boldsymbol{\nabla}p_l + \nu\nabla^2\mathbf{u}_l - \mathcal{P}_l[(\mathbf{u}_l \cdot \boldsymbol{\nabla})\mathbf{u}_l] - \mathcal{P}_l[(\mathbf{u}_l \cdot \boldsymbol{\nabla})\mathbf{u}_h]$$
$$- \mathcal{P}_l[(\mathbf{u}_h \cdot \boldsymbol{\nabla})\mathbf{u}_l] - \mathcal{P}_l[(\mathbf{u}_h \cdot \boldsymbol{\nabla})\mathbf{u}_h] \tag{8a}$$

and

$$\frac{\partial \mathbf{u}_h}{\partial t} + \mathcal{P}_h[(\mathbf{u}_h \cdot \nabla)\mathbf{U}_l] + \mathcal{P}_h[(\mathbf{U}_l \cdot \nabla)\mathbf{u}_h] = -\frac{1}{\rho}\nabla p_h + \nu\nabla^2\mathbf{u}_h - \mathcal{P}_h[(\mathbf{u}_l \cdot \nabla)\mathbf{u}_l] - \mathcal{P}_h[(\mathbf{u}_h \cdot \nabla)\mathbf{u}_h],$$

(8b)

where p_l and p_h are defined to enforce $\nabla \cdot \mathbf{u}_l = 0$ and $\nabla \cdot \mathbf{u}_h = 0$ with $p' = p_l + p_h$. The terms $\mathcal{P}_l[(\mathbf{u}_l \cdot \nabla)\mathbf{u}_h]$ and $\mathcal{P}_h[(\mathbf{u}_h \cdot \nabla)\mathbf{u}_l]$ in (8a) and the self-interaction terms $\mathcal{P}_h[(\mathbf{u}_l \cdot \nabla)\mathbf{u}_l]$ and $\mathcal{P}_h[(\mathbf{u}_h \cdot \nabla)\mathbf{u}_h]$ in (8b) do not appear when the GQL approximation is applied.

C. Spectral energetics

We now address the effect of the GQL approximation on the energetics of the given flow. We note that every term in the mean equation (6a) is constant in uniform shear flow. We first average Eq. (6a) in the wall-normal direction. Multiplying it by dU/dy leads to the following equation for the mean energy balance:

$$I - \nu\left(\frac{dU}{dy}\right)^2 + \langle u'v'\rangle_{x,y,z,t}\frac{dU}{dy} = 0, \quad \text{where} \quad I \equiv \frac{\tau_0}{\rho}\frac{dU}{dy}.$$

(9)

Here I is the energy input originating from the applied shear stress τ_0, and it is balanced with the mean dissipation (second term) and turbulent-kinetic-energy (TKE) production (third term).

The energy transfer is subsequently considered in the Fourier space. To this end, the velocity fluctuation $\mathbf{u}'$ can be written using the one-dimensional continuous Fourier transform

$$u'_j(t, r) = \int_{-\infty}^{\infty} \widehat{u'_j}(t, k)e^{ikr}dk$$

(10)

for $j = 1, 2, 3$, where $\widehat{}$ denotes the Fourier-transformed coefficient, $(u'_1, u'_2, u'_3) = (u', v', w')$, $r(= x \text{ or } z)$ is the streamwise or spanwise coordinate, and $k(= k_x \text{ or } k_z)$ the corresponding wave number. We then take the Fourier transformation (10) to (6b), and multiply it by the complex conjugate of $\widehat{u'_i}(k)$ to give

$$\underbrace{\left\langle \text{Re}\left\{-\overline{\widehat{u'}}\widehat{v'}\frac{dU}{dy}\right\}\right\rangle_{r^\perp, y, t}}_{\widehat{P}(k)} + \underbrace{\left\langle -\nu\frac{\partial\widehat{u'_i}}{\partial x_j}\frac{\partial\overline{\widehat{u'_i}}}{\partial x_j}\right\rangle_{r^\perp, y, t}}_{\widehat{\varepsilon}(k)}$$
$$+ \underbrace{\left\langle \text{Re}\left\{-\overline{\widehat{u'_i}}\left(\frac{\partial}{\partial x_j}(\widehat{u'_i u'_j} - \mathcal{P}_h[\widehat{u'_{h,i}u'_{h,j}}] - \mathcal{P}_h[\widehat{u'_{l,i}u'_{l,j}}]) - \mathcal{P}_l[\widehat{u'_{l,i}u'_{h,j}}] - \mathcal{P}_l[\widehat{u'_{h,i}u'_{l,j}}]\right)\right\}\right\rangle_{r^\perp, y, t}}_{\widehat{T}(k)} = 0,$$

(11)

where $(x_1, x_2, x_3) = (x, y, z)$, $r^\perp(= z \text{ or } x)$ is the horizontal direction orthogonal to r, the overbar indicates the complex conjugate, and $\text{Re}\{\cdot\}$ represents the real part. The statistics in homogeneous shear turbulence are invariant under a translation in the vertical direction, and an average in t and y has further been taken. The terms on the left-hand side are the rate of turbulence production, $\widehat{P}(k)$, viscous dissipation, $\widehat{\varepsilon}(k)$, and (nonlinear) turbulent energy transport, $\widehat{T}(k)$, at given wave numbers, respectively.

Due to the energy-preserving nature of nonlinearity, the turbulent transport integrated over the entire wave numbers is zero:

$$\int_0^\infty \widehat{T}(k)dk = 0.$$

(12)

Therefore, from (11), the production and dissipation exactly balance each other:

$$\int_0^\infty [\widehat{P}(k) + \widehat{\varepsilon}(k)]\, dk = 0. \tag{13}$$

The turbulent kinetic energy equation (11) can further be split into each component:

$$\widehat{P}(k) + \underbrace{\left\langle \mathrm{Re}\left\{ \frac{\widehat{p'}}{\rho} \frac{\partial \widehat{\overline{u'}}}{\partial x} \right\} \right\rangle_{r^\perp, y, t}}_{\widehat{\Pi}_x(k)} + \underbrace{\left\langle -\nu \frac{\partial \widehat{u'}}{\partial x_j} \frac{\partial \widehat{\overline{u'}}}{\partial x_j} \right\rangle_{r^\perp, y, t}}_{\widehat{\varepsilon}_x(k)}$$

$$+ \underbrace{\left\langle \mathrm{Re}\left\{ -\overline{\widehat{u'}} \left(\frac{\partial}{\partial x_j} (\widehat{u'u'_j} - \mathcal{P}_h[\widehat{u'_h u'_{h,j}}] - \mathcal{P}_h[\widehat{u'_l u'_{l,j}}] - \mathcal{P}_l[\widehat{u'_l u'_{h,j}}] - \mathcal{P}_l[\widehat{u'_h u'_{l,j}}]) \right) \right\} \right\rangle_{r^\perp, y, t}}_{\widehat{T}_x(k)} = 0,$$

$$\tag{14a}$$

$$\underbrace{\left\langle \mathrm{Re}\left\{ \frac{\widehat{p}}{\rho} \frac{\partial \widehat{\overline{v'}}}{\partial y} \right\} \right\rangle_{r^\perp, y, t}}_{\widehat{\Pi}_y(k)} + \underbrace{\left\langle -\nu \frac{\partial \widehat{v'}}{\partial x_j} \frac{\partial \widehat{\overline{v'}}}{\partial x_j} \right\rangle_{r^\perp, y, t}}_{\widehat{\varepsilon}_y(k)}$$

$$+ \underbrace{\left\langle \mathrm{Re}\left\{ -\overline{\widehat{v'}} \left(\frac{\partial}{\partial x_j} (\widehat{v'u'_j} - \mathcal{P}_h[\widehat{v'_h u'_{h,j}}] - \mathcal{P}_h[\widehat{v'_l u'_{l,j}}] - \mathcal{P}_l[\widehat{v'_l u'_{h,j}}] - \mathcal{P}_l[\widehat{v'_h u'_{l,j}}]) \right) \right\} \right\rangle_{r^\perp, y, t}}_{\widehat{T}_y(k)} = 0,$$

$$\tag{14b}$$

$$\underbrace{\left\langle \mathrm{Re}\left\{ \frac{\widehat{p'}}{\rho} \frac{\partial \widehat{\overline{w'}}}{\partial z} \right\} \right\rangle_{r^\perp, y, t}}_{\widehat{\Pi}_z(k)} + \underbrace{\left\langle -\nu \frac{\partial \widehat{w'}}{\partial x_j} \frac{\partial \widehat{\overline{w'}}}{\partial x_j} \right\rangle_{r^\perp, y, t}}_{\widehat{\varepsilon}_z(k)}$$

$$+ \underbrace{\left\langle \mathrm{Re}\left\{ -\overline{\widehat{w'}} \left(\frac{\partial}{\partial x_j} (\widehat{w'u'_j} - \mathcal{P}_h[\widehat{w'_h u'_{h,j}}] - \mathcal{P}_h[\widehat{w'_l u'_{l,j}}] - \mathcal{P}_l[\widehat{w'_l u'_{h,j}}] - \mathcal{P}_l[\widehat{w'_h u'_{l,j}}]) \right) \right\} \right\rangle_{r^\perp, y, t}}_{\widehat{T}_z(k)} = 0,$$

$$\tag{14c}$$

where $\widehat{\Pi}_x(k)$, $\widehat{\Pi}_x(k)$, and $\widehat{\Pi}_x(k)$ are the streamwise, wall-normal, and spanwise components of the pressure strain, respectively. These terms do not appear in Eq. (11) because the continuity equation gives

$$\widehat{\Pi}_x(k) + \widehat{\Pi}_y(k) + \widehat{\Pi}_z(k) = 0. \tag{15}$$

Equation (15) indicates that the pressure strain would play an essential role in the distribution of TKE produced at the streamwise component to the others through continuity [50].

D. Numerical simulations

The equations used in this study can be nondimensionalized by the total shear stress τ_0 and the kinematic viscosity ν. Using the friction velocity $u_\tau = \sqrt{\tau_0/\rho}$ and the Kolmogorov length scale $\eta = \nu/u_\tau$ the mean-momentum equation (6a) is obtained as

$$\frac{dU^*}{dy^*} - \langle u'^* v'^* \rangle_{x,z,t} = 1, \tag{16}$$
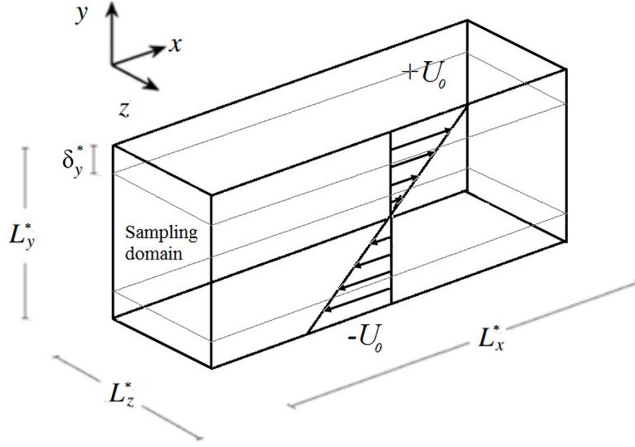
FIG. 1. Flow geometry featuring a sampling domain of size $L_x^* \times (L_y^* - 2\delta_y^*) \times L_z^*$ for simulation of homogeneous shear turbulence.

and the fluctuation equations (6b) are

$$\frac{\partial \mathbf{u}'^*}{\partial t^*} + (\mathbf{U}^* \cdot \boldsymbol{\nabla}^*)\mathbf{u}'^* + (\mathbf{u}'^* \cdot \boldsymbol{\nabla}^*)\mathbf{U}^* = \boldsymbol{\nabla}^* p'^* + \boldsymbol{\nabla}^{*2}\mathbf{u}'^* - (\mathbf{u}'^* \cdot \boldsymbol{\nabla}^*)\mathbf{u}'^*, \qquad (17)$$

where the superscript $(\cdot)^*$ represents the dimensionless variables. The viscous terms in the dimensionless equations are order of unity, which indicates that the velocity and length scales correspond to Kolmogorov scales. The velocity and length scales of the largest eddies admitted are $\Delta U^* = L_z^*$ and L_z^*, where ΔU^* indicates the difference in the mean velocity over the characteristic large-eddy size L_z in the vertical direction. Therefore, $Re_{\tau,L_z} = L_z^* = u_\tau L_z/\nu$ is used to characterize the separation between the largest and smallest length scales in the flow. Direct numerical simulations and simulations of the GQL model for homogeneous shear turbulence are carried out using the approach in [32,43]. Figure 1 shows a schematic diagram explaining how homogeneous shear flow is simulated in the present study. Plane Couette flow is simulated, with two parallel sliding walls with the velocity, $\pm U_0$, at $y = \pm L_y/2$, respectively. The spanwise domain of the simulations is restricted to be $L_z < L_y$ so that the size of largest eddies is determined by L_z. This implies that the effect of the near-wall structures remains confined in the near-wall region, whose thickness will be $O(L_z)$ at best [32,43]. Since the equations of motion of plane Couette flow are identical to those of homogeneous shear flow, this setting allows us to simulate homogeneous shear turbulence in the bulk region. With the aforementioned simulation set-up, the statistics of uniform shear turbulence can now be sampled from the bulk region $y \in [-L_y/2 + \delta_y, L_y/2 - \delta_y]$, where the effect of the walls is negligible (see Fig. 1; δ_y is the cutoff y location for sampling statistics in the bulk region). This can be seen in Fig. 2, where the black dashed line represents the location which separates the bulk region (from where the statistics have been sampled) and the near-wall region (whose effect has been neglected in the present work), and δ_y has been determined by looking at the location where the first-order statistics is constant. For further details of numerical setup in the present study, the reader may refer to [43].

The numerical simulations in the present study are performed using `diablo` [51], which has been validated in a number of previous studies [32,43,52]. The spanwise and streamwise directions are discretized using Fourier series with the 2/3 dealiasing rule, and the wall-normal direction is discretized using a second-order central difference. The time integration is carried out semi-implicitly based on the fractional-step method [53]. The viscous terms are all implicitly advanced with a second-order Crank-Nicolson method, while the rest of the terms are explicitly integrated via a third-order low-storage Runge-Kutta method. These numerical methods are all applied to both
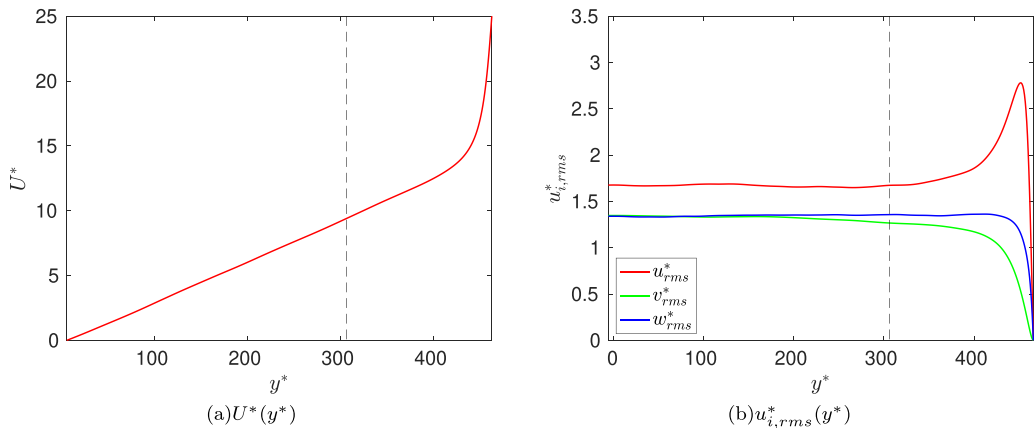
FIG. 2. First- and second-order turbulence statistics (DNS) for $y^* \in [0, L_y^*/2]$. The sampling domain is delimited by the solid vertical line separating the bulk from the near-wall region. (a) $U^*(y^*)$; (b) $u_{\rm rms}^*$, $v_{\rm rms}^*$ and $w_{\rm rms}^*$.

QL/GQL and DNS, and the only difference is in the setup of the nonlinear terms: a decomposition is further introduced, and each set of terms is added to solve the corresponding equations for $\mathbf{U}_l$ and $\mathbf{u}_h$.

Table I summarizes the parameters for the numerical simulations performed in the present study. The simulations have been divided into DNS, QL, and GQL cases. The Reynolds number considered here for all simulations is $\mathrm{Re}[\equiv U_0 L_y/(2\nu)] = 13\,000$, and the friction Reynolds number is $\mathrm{Re}_{\tau,L_z} \approx 279$ (DNS). The horizontal computational box size is $L_x \times L_z = 1.8 L_y \times 0.6 L_y$. The streamwise/spanwise domain's aspect ratio has been chosen to be $L_x/L_z = 3$, in line with [32,42]. The number of grid points is $N_x \times N_y \times N_z = 96 \times 305 \times 64$ in the x, y, and z directions, respectively. The total number of Fourier modes in the streamwise and spanwise wave-number space is $M_{x,F} \times M_{z,F} = 32 \times 21$. The threshold streamwise and spanwise wavelength for the decomposition

TABLE I. Simulation parameters in the present study. The Reynolds number based on the friction velocities is $\mathrm{Re}_{\tau,L_z} = L_z^*$. The grid spacings in the x and z directions are Δ_x^* and Δ_z^* (after dealiasing). $\lambda_{x,c}$ and $\lambda_{z,c}$ are the threshold streamwise and spanwise wavelengths, respectively. The number of the positive-wave-number streamwise Fourier modes is denoted by $M_{x,F}$, and the number of the positive-wave-number spanwise Fourier modes is $M_{z,F}$. The number of grid points in the x, y, and z directions is denoted by N_x, N_y, and N_z, respectively.

Case	Re_{τ,L_z}	Δx^*	Δz^*	$\lambda_{x,c}$	$\lambda_{z,c}$	$\lambda_{x,c}^*$	$\lambda_{z,c}^*$	$M_{x,F}$	$M_{z,F}$	$N_x \times N_y \times N_z$	δ_y^*	$T_{\rm stats}^*$
DNS	279	13.1	6.5	—	—	—	—	32	21	$96 \times 305 \times 64$	306	143 159
QLX	350	16.4	8.2	0	—	0	—	0	21	$96 \times 305 \times 64$	383	572 514
NX2	282	13.2	6.6	0.90	—	423	—	2	21	$96 \times 305 \times 64$	309	382 212
NX4	281	13.2	6.6	0.45	—	211	—	4	21	$96 \times 305 \times 64$	308	441 833
NX7	266	12.5	6.2	0.26	—	115	—	7	21	$96 \times 305 \times 64$	291	343 407
QLZ	285	13.4	6.7	—	0	—	0	32	0	$96 \times 305 \times 64$	311	446 294
NZ2	265	12.4	6.2	—	0.30	—	133	32	2	$96 \times 305 \times 64$	290	556 391
NZ4	266	12.5	6.2	—	0.15	—	66.5	32	4	$96 \times 305 \times 64$	292	366 187
NZ7	273	12.8	6.4	—	0.09	—	39.0	32	7	$96 \times 305 \times 64$	299	81 058
N22	291	13.6	6.8	0.90	0.30	437	146	2	2	$96 \times 305 \times 64$	319	224 863
N44	289	13.5	6.8	0.45	0.15	217	72.3	4	4	$96 \times 305 \times 64$	316	240 244
N77	271	12.7	6.4	0.26	0.09	116	38.7	7	7	$96 \times 305 \times 64$	296	297 831

TABLE II. Turbulence statistics in the present study. dU^*/dy^* and $-\langle u'^* v'^* \rangle$ are the two components of mean-momentum equation. u^*_{rms}, v^*_{rms}, and w^*_{rms} are the root-mean-squared velocities of streamwise, vertical, and spanwise velocities of fluctuations, respectively.

Simulation	Re_λ	dU^*/dy^*	$-\langle u'^* v'^* \rangle$	u^*_{rms}	v^*_{rms}	w^*_{rms}
DNS	47	0.03	0.97	1.66	1.32	1.34
QLX	79	0.01	0.99	1.77	1.35	1.23
NX2	47	0.03	0.97	1.68	1.33	1.36
NX4	50	0.03	0.97	1.70	1.41	1.37
NX7	42	0.04	0.96	1.68	1.35	1.33
QLZ	58	0.03	0.97	1.77	1.51	1.56
NZ2	48	0.04	0.96	1.75	1.43	1.39
NZ4	45	0.04	0.96	1.73	1.36	1.33
NZ7	46	0.04	0.96	1.73	1.36	1.35
N22	53	0.03	0.97	1.70	1.38	1.35
N44	49	0.03	0.97	1.67	1.36	1.31
N77	43	0.04	0.96	1.68	1.34	1.28

of the velocity into the two groups in (1) is given by $\lambda_{r,c} = 2\pi/k_{r,c}$ with $k_{r,c} = 2\pi M_{r,F}/L_r$, where $r = x, z$ is the streamwise or spanwise directions, respectively. The time interval for sampling of statistics is denoted by T^*_{stats}. The DNS case resolves all Fourier modes in both directions, up to the resolution used (Table I). The QLX (QLZ) case resolves the first streamwise (spanwise) Fourier mode in the first group, whereas the remaining streamwise (spanwise) modes are linearized about the former, and all spanwise (streamwise) Fourier modes are included in the first (nonlinear) group. The NX no. (NZ no.) cases (no. $= 2, 4, 7$) are the GQL simulations in which the first (no. $+ 1$) streamwise (spanwise) Fourier mode is included in the first group. Finally, the N no. cases are GQL simulations with different combinations of modes that have been explored, and the results are reported in Sec. III.

III. RESULTS

A. Turbulence statistics and spectra

We first consider the set of DNS, QL, and GQL simulations in Tables I and II. The QL model (QLX case) exhibits higher Re_{τ,L_z} than DNS. As more streamwise modes are included in the $\mathcal{P}_l$-subspace group (NX no. cases, where no. $= 2, 4, 7$), Re_{τ,L_z} is further reduced. The QL model also displays a higher Re_λ compared to DNS. From (6a), this implies that the energy input given to the flow is increased by the QL approximation: if the flow in the QL model is more turbulent, the contribution of the Reynolds shear-stress term in (16) should also increase, leading to a decrease of dU^*/dy^* as observed in Table II and consistent with Ref. [32]. The QLZ and subsequent NZ no. cases exhibit a different behavior: QLZ sees a very small increase in Re_{τ,L_z} with respect to DNS, while the NZ no. cases show an increase with the number of spanwise modes (opposite to the NX no. trend). The inclusion of two more spanwise modes in the $\mathcal{P}_l$-subspace group is found to increase Re_{τ,L_z} of the NZ no. cases, except for the case with eight spanwise modes, where a decreasing trend is observed.

The first- and second-order statistics in the bulk region can be found in Table II. The QL model (QLX) is found to generate more anisotropic velocity fluctuations, in particular, u^*_{rms} and v^*_{rms} are increased while w^*_{rms} is decreased. This behavior is consistent with the previous study [32] at lower and higher Reynolds numbers than that considered here and differs from the channel flow case [30,35,54], where only u^*_{rms} is increased by the QL approximation while the other turbulence statistics are decreased. As $M_{x,F}$ is increased from the QLX case (NX no. case), the value of v^*_{rms} relative to u^*_{rms} increases nonmonotonically. A similar trend is seen from w^*_{rms}. Similar one-point

turbulence statistics is found in the NX7 case compared to DNS. It is interesting to note that the statistics of the NX2 case also shows excellent agreement with that of DNS, but the NX4 case does not exhibit such a behavior. This issue will be discussed in detail in Sec. IV A.

The cases of QL/GQL approximation made in the spanwise direction are found to exhibit relatively larger velocity fluctuations than those in the streamwise direction: the QLZ case sees all $u_{\rm rms}^*$, $v_{\rm rms}^*$, and $w_{\rm rms}^*$ increased. As $M_{z,F}$ is increased, the values of the velocity fluctuations approach those of DNS (NZ no.); in particular, $v_{\rm rms}^*$ and $w_{\rm rms}^*$ of the NZ4 and NZ7 cases give the closest match of statistics to DNS. This represents a difference to the NX no. cases: a larger number of spanwise Fourier modes need to be retained in the $\mathcal{P}_l$-subspace group to obtain velocity fluctuations that match those of DNS. The statistics of the combined cases (N no. cases) displays various trends, but its convergence to the DNS statistics appears to be slightly better than NX and NZ no. cases.

Figure 3 compares the premultiplied spanwise wave-number spectra of Reynolds normal stress (focus on Φ_{uu}^* and Φ_{vv}^*) of DNS with those of the QL/GQL approximation in the streamwise direction [QLX, NX2, NX4, and NX7; Figs. 3(a) and 3(b)], in the spanwise direction [QLZ, NZ2, NZ4, and NZ7; Figs. 3(c) and 3(d)], and with combined cases [N22, N44, and N77; Figs. 3(e) and 3(f)]. The streamwise velocity component of the QLX case displays increased spectral energy intensity over almost the whole range of spanwise wave numbers [Fig. 3(a)], except at largest scales ($k_z L_z \lesssim 8$). It is also observed that the QLX case shows an increased spectral energy of the wall-normal Reynolds stress spectra at large scale [$k_z L_z \lesssim 10$; Fig. 3(b)]. However, these spectra of the QLX case fall off more quickly than those of DNS at high spanwise wave numbers. All these trends are consistent with the results for the QL model reported in [32]. As $M_{x,F}$ is increased, the spectral energy becomes closer to that of DNS. In particular, the NX4 case shows excellent resemblance except at the largest scales, where the differences are the greatest. The spectral energy of the QLZ case is found to be elevated and retained within a limited range of spanwise wave numbers ($k_z L_z \lesssim 18$), after which they fall to zero very quickly, for all velocity components [Figs. 3(c) and 3(d)]. This is due to the absence of energy cascade along the spanwise direction, along which the QL approximation has been carried out, and will be discussed further with Fig. 6. As $M_{z,F}$ is increased, the GQL cases display a greater range of wave numbers with nonnegligible spectral energy; in particular NZ2 is active in the range $k_z L_z \lesssim 18$, NZ4 in $k_z L_z \lesssim 31$, and NZ7 in $k_z L_z \lesssim 50$. These approximately correspond to the cutoff spanwise wavelengths (see Table II). The spectra of the combined cases show a decreased spectral energy intensity at large scales [Figs. 3(e) and 3(f)]. The spectra display "bumps" in which the spectral energy decreases abruptly at spanwise wave numbers corresponding to the cutoff for every case (Table II); however, these drops are not absolute, and there still remains nonnegligible energy after them. We note that the turbulent state generated by the GQL cases is supported by a $\mathcal{P}_l$ subspace composed of Fourier modes in both streamwise and spanwise wave-number space, and it appears that this feature enables a nonnegligible amount of energy to be transferred, unlike in Figs. 3(c) and 3(d). This behavior is also observed in the streamwise wave-number spectra (Fig. 4) and will be discussed below.

Figure 4 shows the premultiplied streamwise wave-number spectra of the Reynolds stress of DNS and QL/GQL models. The spectral energy of the QLX case is found to be larger than that of the DNS at large scales ($k_x L_z \lesssim 6$), while it quickly falls to zero before reaching $k_x L_z \approx 10$ [Figs. 4(a) and 4(b)]. This indicates that the energy contained in the zeroth streamwise Fourier mode could not be redistributed from large- to small-scale motions in streamwise wave-number space, and the energy transport is halted in this direction due to the QL approximation. This behavior is consistent with previous studies [32,34,35,54]. It should be noted that the role of the self-interacting nonlinear term in (8b) is the coupling between streamwise Fourier modes of (8b). Therefore, its removal by the QL approximation leads to the halt of turbulent energy transport (11) and inhibits the related energy cascade in the streamwise direction, as will be shown in Sec. III B. As $M_{x,F}$ is increased, the spectral energy becomes closer to that of DNS; in particular NX7 shows good resemblance at large scales. It is observed that the spectral energy of NX2 does not drop to zero over the entire streamwise wave-number space, largely improving the spectral behavior of the QL model by just incorporating two more modes in the $\mathcal{P}_l$-subspace group. However, the spectral energy of NX4 and

(a)$k_z L_z \Phi_{uu}^*(k_z L_z)$

(b)$k_z L_z \Phi_{vv}^*(k_z L_z)$

(c)$k_z L_z \Phi_{uu}^*(k_z L_z)$

(d)$k_z L_z \Phi_{vv}^*(k_z L_z)$

(e)$k_z L_z \Phi_{uu}^*(k_z L_z)$
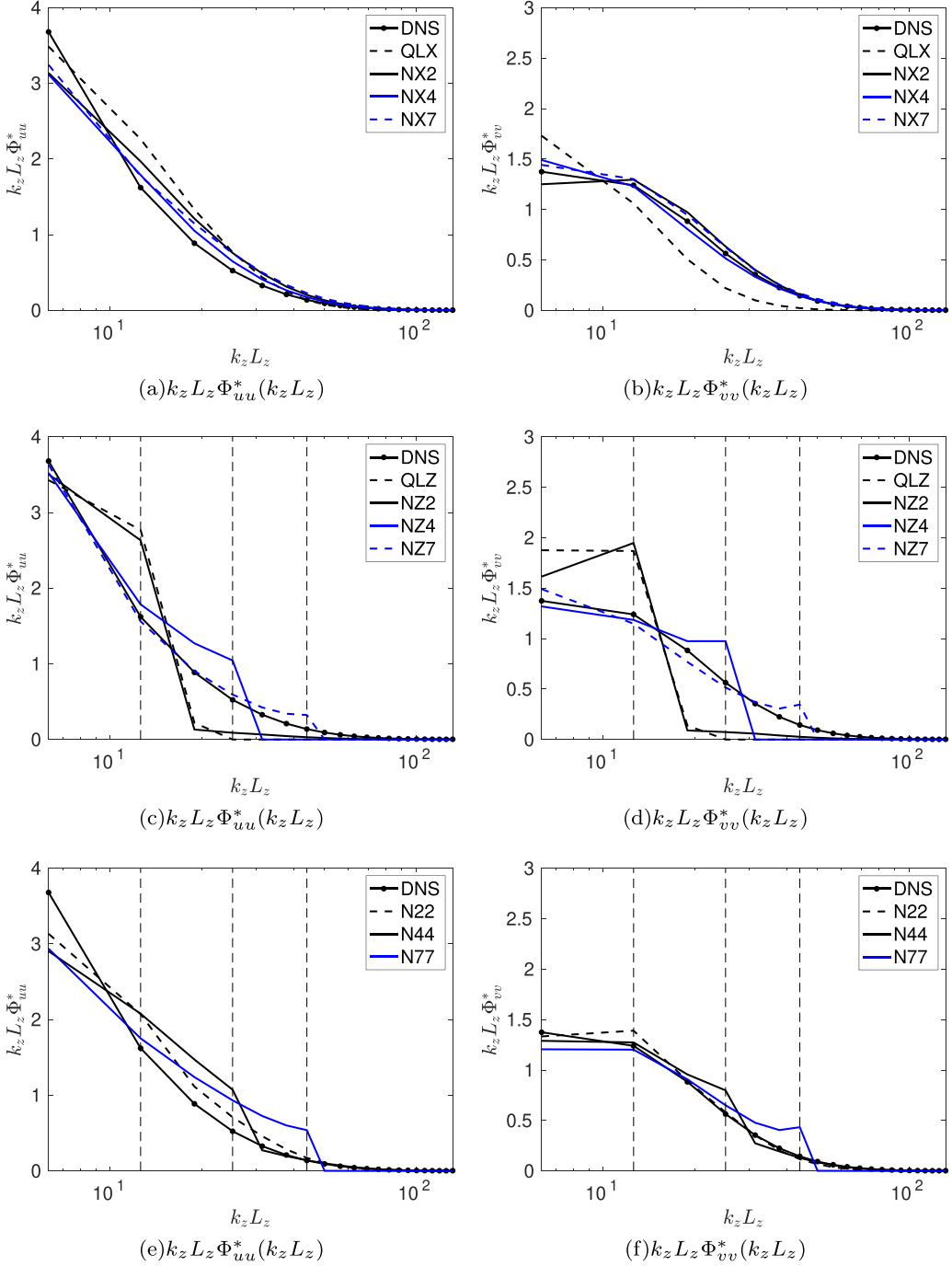
(f)$k_z L_z \Phi_{vv}^*(k_z L_z)$

FIG. 3. Premultiplied spanwise wave-number spectra of Reynolds stresses of DNS, QL, and GQL models. (a, c, e) $k_z L_z \Phi_{uu}^*(k_z L_z)$ and (b, d, f) $k_z L_z \Phi_{vv}^*(k_z L_z)$. The vertical lines represent the spanwise cutoff wave numbers ($k_{z,c}$) dividing the $\mathcal{P}_h$- (right) and $\mathcal{P}_l$-subspace (left) regions.
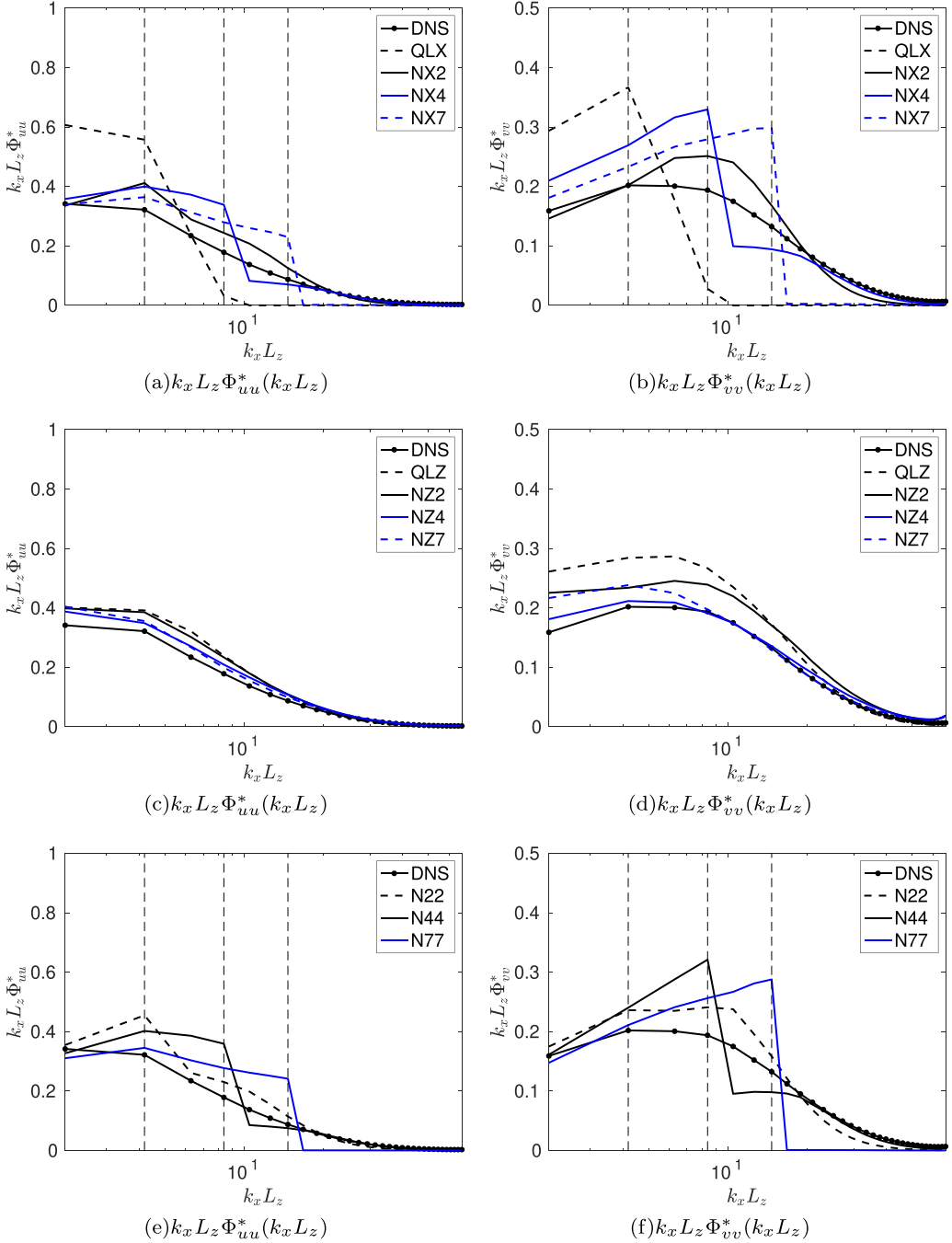
FIG. 4. Premultiplied streamwise wave-number spectra of Reynolds stresses of DNS, QL, and GQL models. (a, c, e) $k_x L_z \Phi_{uu}^*(k_x L_z)$ and (b, d, f) $k_x L_z \Phi_{vv}^*(k_x L_z)$. The vertical lines represent the streamwise cutoff wave numbers ($k_{x,c}$) dividing the $\mathcal{P}_h$- (right) and $\mathcal{P}_l$-subspace (left) regions.

NX7 show partial and total drops at approximately their cutoff streamwise wavelength, respectively. In contrast, the QLZ case exhibits spectra extending over all streamwise wave numbers, despite the larger spectral energy for all four components of the Reynolds shear stress [Figs. 4(c) and 4(d)]. The NZ4 case appears to give the closest spectra compared to DNS, while NZ7 gives the greatest differences. Last, Figs. 4(e) and 4(f) show that the combined GQL cases in the streamwise and spanwise directions exhibit spectra are similar to those of their NX no. counterpart cases; note the resemblance between N22 and NX2, between N44 and NX4, and between N77 and NX7.

Figure 5 shows a visualization of instantaneous streamwise and wall-normal velocity fields of DNS and QL/GQL simulation cases. For the DNS case, the motions associated with the streamwise velocity fluctuation (blue isosurface) tend to be elongated in the streamwise direction, while those corresponding to the wall-normal velocity fluctuations (red isosurface) appear to be more isotropic. The flow field of the QLX case differs in that both motions appear to be elongated in the streamwise direction. This case clearly features the motions associated to the self-sustaining process, which are retained by the QL approximation in the streamwise direction. This is not the case with QLZ, whose flow field does not clearly feature large-scale structures elongated in the streamwise direction. The GQL cases, however, exhibit smaller-scale structures, with flow fields that resemble that of DNS.

B. Spectral energy transfer

Now we study the spectral energy transfer in DNS, QLX, QLZ, and GQL cases. Owing to the balance between production and dissipation given in (13), the spectral energy density of each term in (11) is expected to be dependent on the rate of production of each simulation case. For this reason, we consider the spectral energy budget per unit mean shear $\widehat{P}^*/(dU^*/dy^*)$, $\widehat{T}^*/(dU^*/dy^*)$ and $\widehat{\varepsilon}^*/(dU^*/dy^*)$ like in [32]. By doing so, the inner-scaled turbulence production per unit mean shear is now controlled to be $P^*/(dU^*/dy^*) \simeq 1$ for all the cases (see Table II), making the comparison between the cases more sensible.

The premultiplied spanwise wave-number spectra of the production, turbulent transport and dissipation per unit mean shear for the selected cases are plotted in Fig. 6. All the plots on the left column [Figs. 6(a), 6(c), 6(e), 6(g)] show a qualitatively similar behavior: production takes place at large scales ($k_z L_z \lesssim 30$) and redistributes the energy to turbulent transport and viscous dissipation. At small scales ($k_z L_z \gtrsim 50$), the production becomes negligible and the turbulent transport is exactly balanced with the viscous dissipation. The spectra of the QLX case are qualitatively similar to those of DNS, but their spectral intensity is overall slightly higher. There are, however, subtle differences in the spectral extent for the simulation cases: the transport and dissipation spectra diminish at $k_z L_z \simeq 130$ for DNS [Figs. 6(a) and 6(b)], whereas those of QLX do the same only at $k_z L_z \simeq 80$ [Fig. 6(c)]. This is consistent with the spectra of Φ^*_{uu} and Φ^*_{vv} in Fig. 3, where the spectral intensities at high spanwise wave number of QLX are shown to be smaller than those of DNS. As $M_{x,F}$ is increased, the range of the spanwise wave-number extent of the spectra is found to approximately reach that of DNS with only two more streamwise Fourier modes in the $\mathcal{P}_l$-subspace group, i.e., NX2 [Fig. 6(e)]. In contrast, the spectra of the QLZ case are found not to develop the typical features of energy cascade and turbulent dissipation observed in the QLX case. In particular, both turbulent transport and dissipation spectra are highly localized within the wave-number space where the production is active: i.e., $k_z L_z \lesssim 20$ [Fig. 6(d)]. This explains the sudden drop of both Φ^*_{uu} and Φ^*_{vv} at the aforementioned wave number [Figs. 3(c) and 3(d)]. As expected, the QL approximation in the spanwise direction strongly damages the spanwise energy cascade. As $M_{z,F}$ is increased by a few spanwise Fourier modes (NZ2), the spectra are shown to extend over a wider range of spanwise wave numbers [Fig. 6(f)]. However, the situation changes when more modes are added to the $\mathcal{P}_l$-subspace group [Fig. 6(h)]: the spectra of NZ7 show a sudden drop of turbulent transport at $k_z L_z \simeq 50$, reminiscent of the complete depletion of energy observed in the $\mathcal{P}_h$-subspace region observed in [35,36]. This issue will be discussed in detail in Sec. IV.
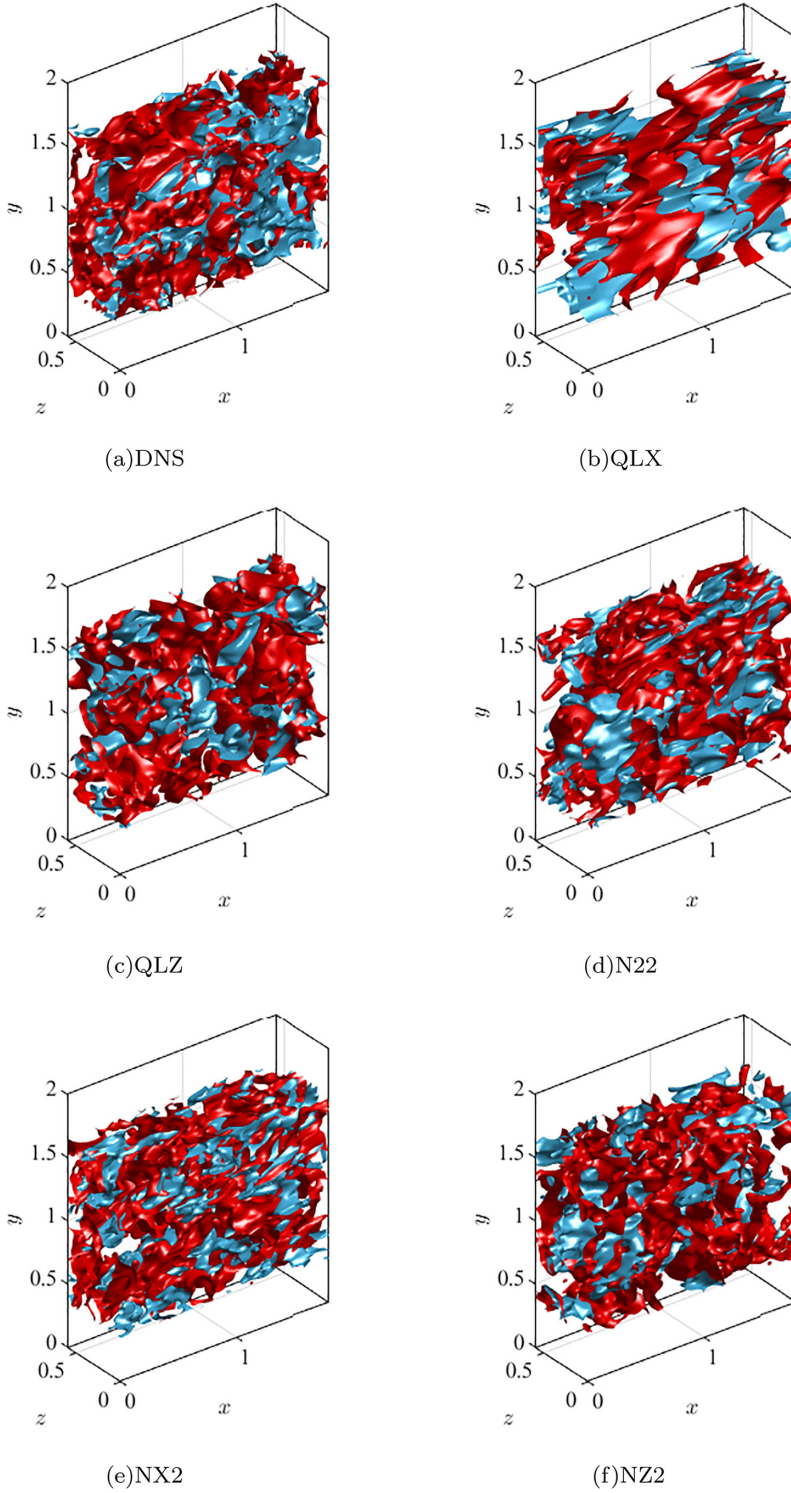
FIG. 5. Instantaneous flow fields of the DNS and QL/GQL simulations. The blue isosurfaces indicate $u'^* = 2$, while the red ones are $v'^* = 0.5$.
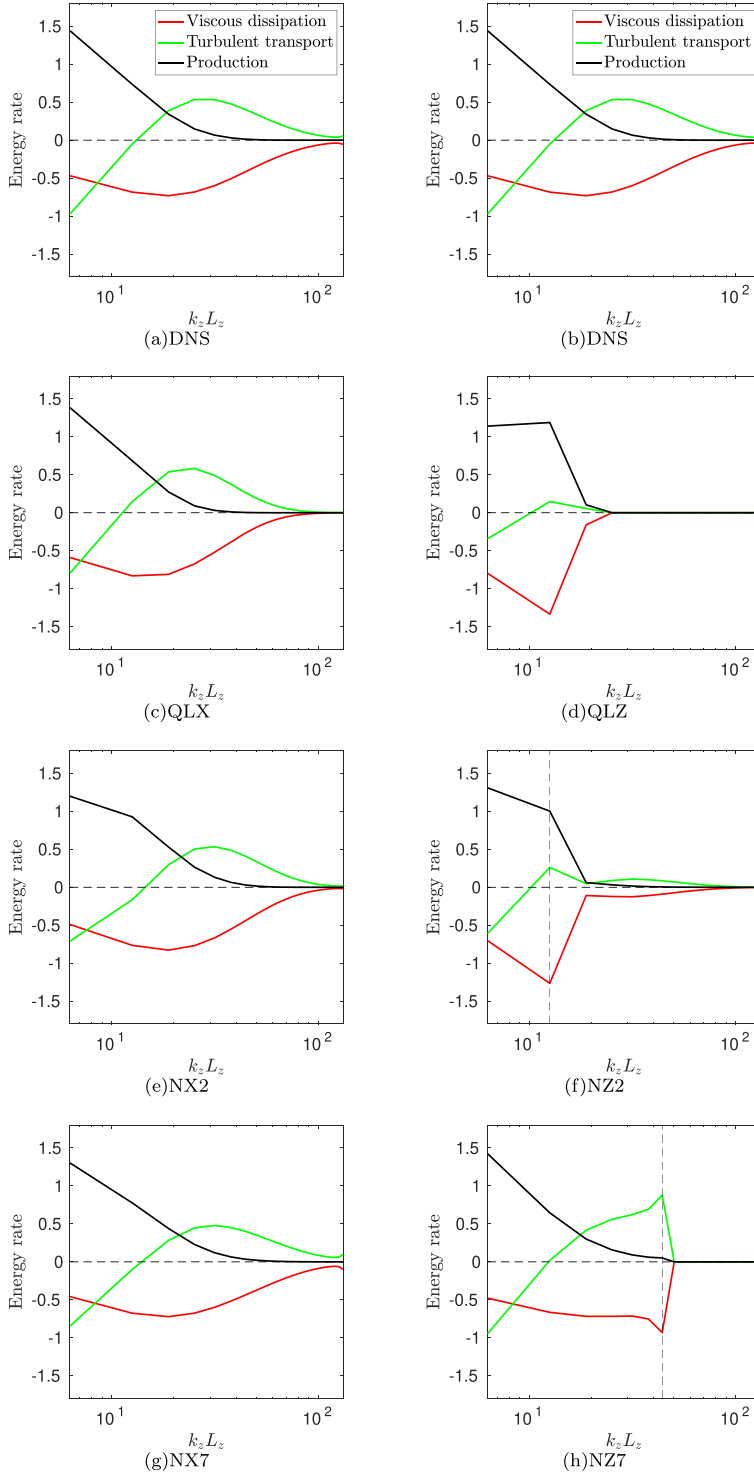
FIG. 6. Premultiplied spanwise wave-number spectra of energy budget per unit mean shear: (a, b) DNS; (c) QLX; (d) QLZ; (e) NX2; (f) NZ2; (g) NX7; (h) NZ7. The vertical lines represent the spanwise cutoff wave numbers ($k_{z,c}$) dividing the $\mathcal{P}_h$- (right) and $\mathcal{P}_l$-subspace (left) regions.

The premultiplied streamwise wave-number spectra of the energy budget per unit mean shear are shown in Fig. 7. The production takes place at large scales ($k_x L_z \lesssim 20$) and is transferred into the turbulent transport and viscous dissipation. The QLX case exhibits a disruption of the energy cascade at $k_x L_z \gtrsim 10$, and an increased spectral energy is observed at large scales, compared to DNS [Fig. 7(c)]. As $M_{x,F}$ is increased, the spectra of the NX2 case show a recovery of the energy cascade in the streamwise direction, extending over a wider range of streamwise wave numbers and matching the DNS spectra fairly well [Fig. 7(e)]. In particular, comparing these streamwise energy-budget spectra with the spanwise counterparts of NZ2 [Fig. 6(f)] suggests that the quasilinear approximation in the streamwise direction seems to offer a scattering mechanism that provides a better energy transfer from the $\mathcal{P}_l$- to the $\mathcal{P}_h$-subspace group. We note that the QLX case has been understood as a minimal model for SSP, as the streamwise wave resolved by its high-wave-number group is modeled with the linearized equations about the streamwise uniform "streaky" flow. In this respect, NX2 perhaps offers a minimal description on the nonlinear evolution of the streamwise wave, which is often believed to be crucial for the regeneration of streamwise vortices [40,55–57], and this may explain why the scattering mechanism of NX2 performs better than that of NZ2. The spectra of the NX7 case show a sharp drop of the spectral energy at $k_x L_z \simeq 18$, in agreement with the trends displayed by the spectra of Φ_{uu}^* and Φ_{vv}^* (Fig. 3), and this is also similar to the NX7 case whose $\mathcal{P}_h$-subspace group showed a depletion of the spectral energy. It is interesting to note that, due to this behavior, the streamwise wave-number energy-budget spectra of the NX7 case appear to be considerably different from DNS, unlike the NX2 case. Last, the QLZ case exhibits a reasonably active cascade in the streamwise direction, as it appears to reasonably well reproduce the streamwise wave-number spectra of DNS. The spectra of the GQL cases NZ2 and NZ7 also show the same behaviors.

C. Componentwise energy transport and pressure strain

The pressure-strain spectra are also analyzed to understand the mechanism of componentwise TKE distribution in the selected QL/GQL cases. The premultiplied spanwise wave-number spectra of the pressure-strain transport terms for the DNS, QLX, QLZ, and GQL cases are shown in Fig. 8. The DNS shows a negative streamwise component of the pressure strain Π_x^*, while Π_y^* and Π_z^* are positive for the most part of the spectra [Figs. 8(a) and 8(b)]. The spectra of QLX show some important differences from those of DNS. In particular, despite that the energy transfer in the spanwise direction is not directly modified by the approximation of QLX, the spectral energy is found to be significantly reduced over then entire range of $k_z L_z$, and the Π_z^* component also becomes negative for $k_z L_z \lesssim 10$ [Fig. 8(c)]. As $M_{x,F}$ is increased [Figs. 8(e) and 8(g)], the spanwise wave-number spectra of NX2 and NX7 exhibit greater spectral energy and extend over larger wave numbers. Similarly to QLX, QLZ also exhibits significantly disrupted spectra for $k_z L_z \approx 20$ [Fig. 8(d)]. In this case, the spectral energy of Π_x^* and Π_z^* is, however, overestimated, and the Π_y^* component is abnormally small and positive over the whole range of spanwise wave numbers. As $M_{z,F}$ is increased, the spectra of NZ2 show a slight extension of the supported spanwise wave numbers. This is further improved in NZ7, except for a sudden drop of spectral energy at the cutoff wavelength of NZ7.

To understand this, let us introduce the following equations for pressure fluctuation [58,59]:

$$\frac{1}{\rho}\nabla^2 p^R = -2\frac{dU}{dy}\frac{\partial v'}{\partial x}, \tag{18a}$$

$$\frac{1}{\rho}\nabla^2 p^S = -\frac{\partial u_j'}{\partial x_i}\frac{\partial u_i'}{\partial x_j}, \tag{18b}$$

where $p' = p^R + p^S$, and p^R and p^S are rapid and slow pressures, respectively. The terms rapid and slow are derived from the fact that only the rapid part responds immediately to a change imposed
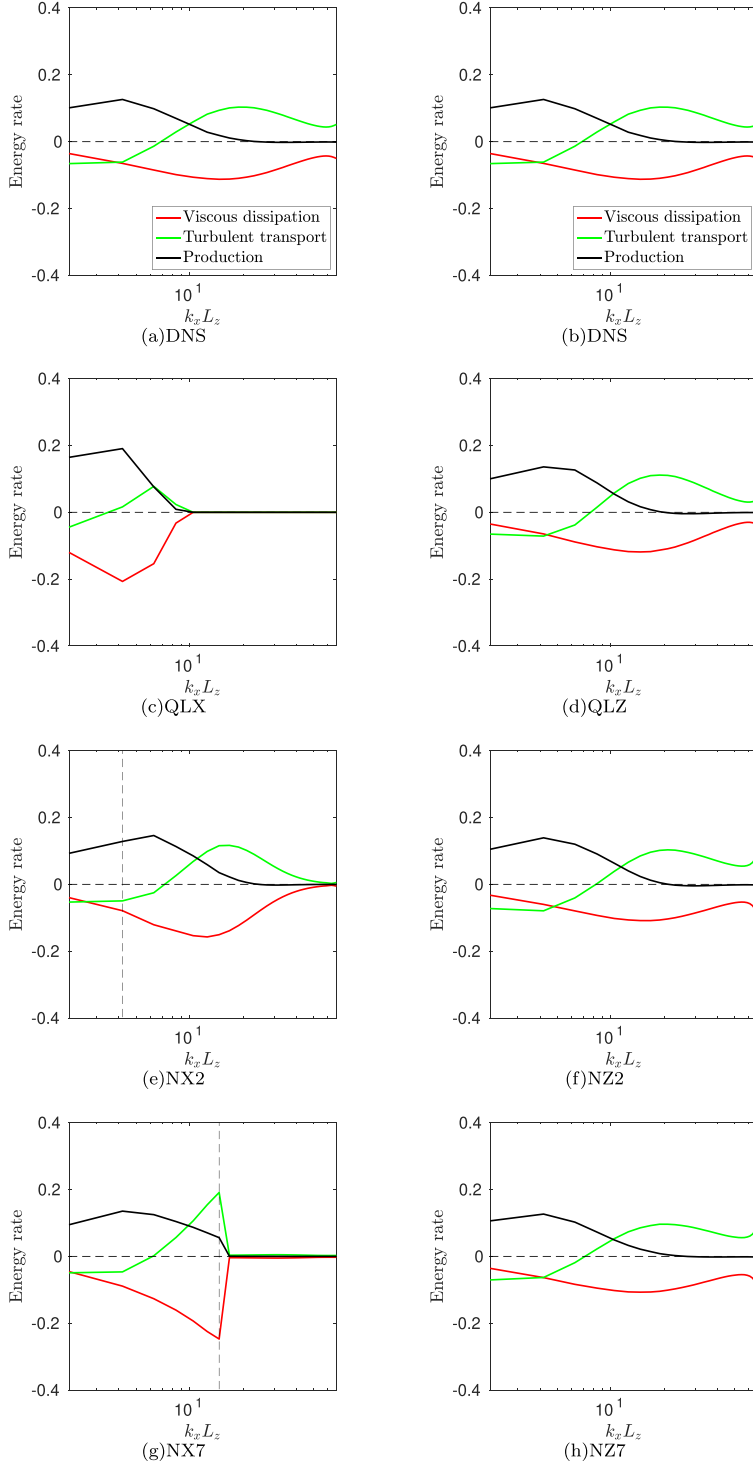
FIG. 7. Premultiplied streamwise wave-number spectra of energy budget per unit mean shear: (a, b) DNS; (c) QLX; (d) QLZ; (e) NX2; (f) NZ2; (g) NX7; (h) NZ7. Here the vertical lines represent the streamwise cutoff wave numbers ($k_{x,c}$) dividing the $\mathcal{P}_h$- (right) and $\mathcal{P}_l$-subspace (left) regions.
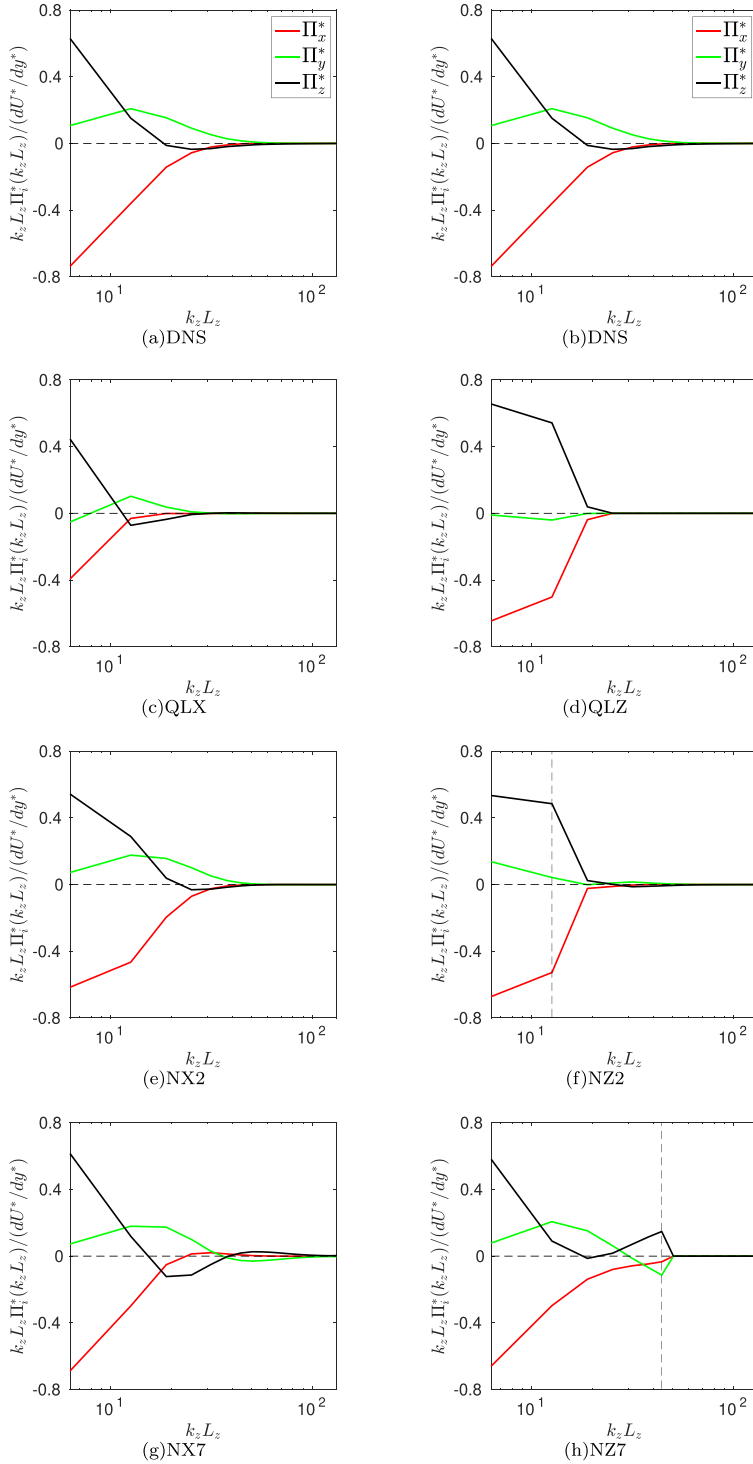
FIG. 8. Premultiplied spanwise wave-number spectra of the pressure-strain transport: (a, b) DNS; (c) QLX; (d) QLZ; (e) NX2; (f) NZ2; (g) NX7; (h) NZ7. Here the vertical lines represent the spanwise cutoff wave numbers ($k_{z,c}$) dividing the $\mathcal{P}_h$- (right) and $\mathcal{P}_l$-subspace (left) regions.

on the mean, and the slow part feels the change through nonlinear interactions [59]. Using the field decomposition in (1) and the projections defined in (2), (18) can be written as

$$\frac{1}{\rho}\nabla^2 p_l^R = -2\frac{dU}{dy}\frac{\partial v_l}{\partial x}, \tag{19a}$$

$$\frac{1}{\rho}\nabla^2 p_l^S = \mathcal{P}_l\left[-\frac{\partial u_{l,j}}{\partial x_i}\frac{\partial u_{l,i}}{\partial x_j}\right] + \mathcal{P}_l\left[-2\frac{\partial u_{l,j}}{\partial x_i}\frac{\partial u_{h,i}}{\partial x_j}\right] + \mathcal{P}_l\left[-\frac{\partial u_{h,j}}{\partial x_i}\frac{\partial u_{h,i}}{\partial x_j}\right], \tag{19b}$$

in the $\mathcal{P}_l$ subspace and

$$\frac{1}{\rho}\nabla^2 p_h^R = -2\frac{dU}{dy}\frac{\partial v_h}{\partial x}, \tag{20a}$$

$$\frac{1}{\rho}\nabla^2 p_h^S = \mathcal{P}_h\left[-\frac{\partial u_{l,j}}{\partial x_i}\frac{\partial u_{l,i}}{\partial x_j}\right] + \mathcal{P}_h\left[-2\frac{\partial u_{l,j}}{\partial x_i}\frac{\partial u_{h,i}}{\partial x_j}\right] + \mathcal{P}_h\left[-\frac{\partial u_{h,j}}{\partial x_i}\frac{\partial u_{h,i}}{\partial x_j}\right], \tag{20b}$$

in the $\mathcal{P}_h$ subspace. In the QL and GQL models, the second term in the right-hand side of (19b) and the first and the last terms in the right-hand side of (20b) are absent. It is therefore evident that the QL/GQL models do not fully account for the slow pressure, which originates from the nonlinear term of turbulent fluctuation equations (6b), thereby playing an important role in energy cascade [32,35,36]. In particular, the decomposition of velocity fluctuations into a streamwise mean and the remaining fluctuation in the case of the QL model (QLX) make $u_{l,j}$ in (20b) not vary in the streamwise direction; thus each streamwise Fourier mode of p_h^S is coupled only with that of $u_{h,j}$ at the same wave number. Therefore, p_h^S does not play any role in the energy transport between the streamwise Fourier modes (32,35). In the GQL model, $u_{l,j}$ is instead allowed to vary in the streamwise direction, which evidently enhances the streamwise-dependent slow pressure generation in the $\mathcal{P}_l$ subspace through (19b). However, even if no approximation is made in the spanwise direction, the QLX case still features lower spectral intensity of pressure strain along the same direction, compared to DNS [Fig. 8(c)]. The reduction of pressure-strain transport even at the integral length scales suggests that the damaged nonlinear terms (through a limited interaction between streamwise Fourier modes) play an important interactive role in the process of turbulence production.

Figure 9 shows the premultiplied streamwise wave-number spectra of the pressure-strain transport. All three components of the pressure-strain transport term of DNS are active down to small scales $k_x L_z \lesssim 40$ in DNS [Figs. 9(a) and 9(b)]. The streamwise wave-number spectra of QLX overall display lower energy like its spanwise counterpart [Fig. 9(c)]. A pronounced spectral cutoff appears at $k_x L_z \approx 9$, beyond which the pressure-strain transport is not active, consistent with Fig. 7(c). With an increase of $M_{x,F}$, the spectra of NX2 extend over larger streamwise wave numbers and appear to match well those of DNS [Fig. 9(e)]. The NX7, however, exhibits a severe drop of spectral energy approximately at the cutoff wavelength ($k_x L_z \approx 18$) [Fig. 9(g)]. The QLZ case shows more energetic pressure-strain transport spectra [Fig. 9(g)], also consistent with the behavior of the spectral energy-budget spectra observed in spanwise direction [Fig. 7(c)]. This case also displays an active energy cascade in streamwise wave-number space. When $M_{z,F}$ is increased, the spectral energy of the Π_x^* and Π_z^* components gets reduced while Π_y^* increases to DNS levels for the NZ2 and NZ7 cases [Figs. 7(f) and 7(h)].

IV. DISCUSSION

In the present work, the generalized quasilinear (GQL) approximation in both the streamwise and spanwise directions has been applied to homogeneous shear turbulence. This study is the direct extension of the previous work on the QL approximation [32]. For the GQL approximation in this study, the flow is decomposed into a group of low-wave-number Fourier modes ($\mathcal{P}_l$ subspace) and the rest ($\mathcal{P}_h$ subspace) as in (1), the former of which is solved by considering the full nonlinear equations, whereas the latter is obtained by solving the linearized equations about the former. Unlike
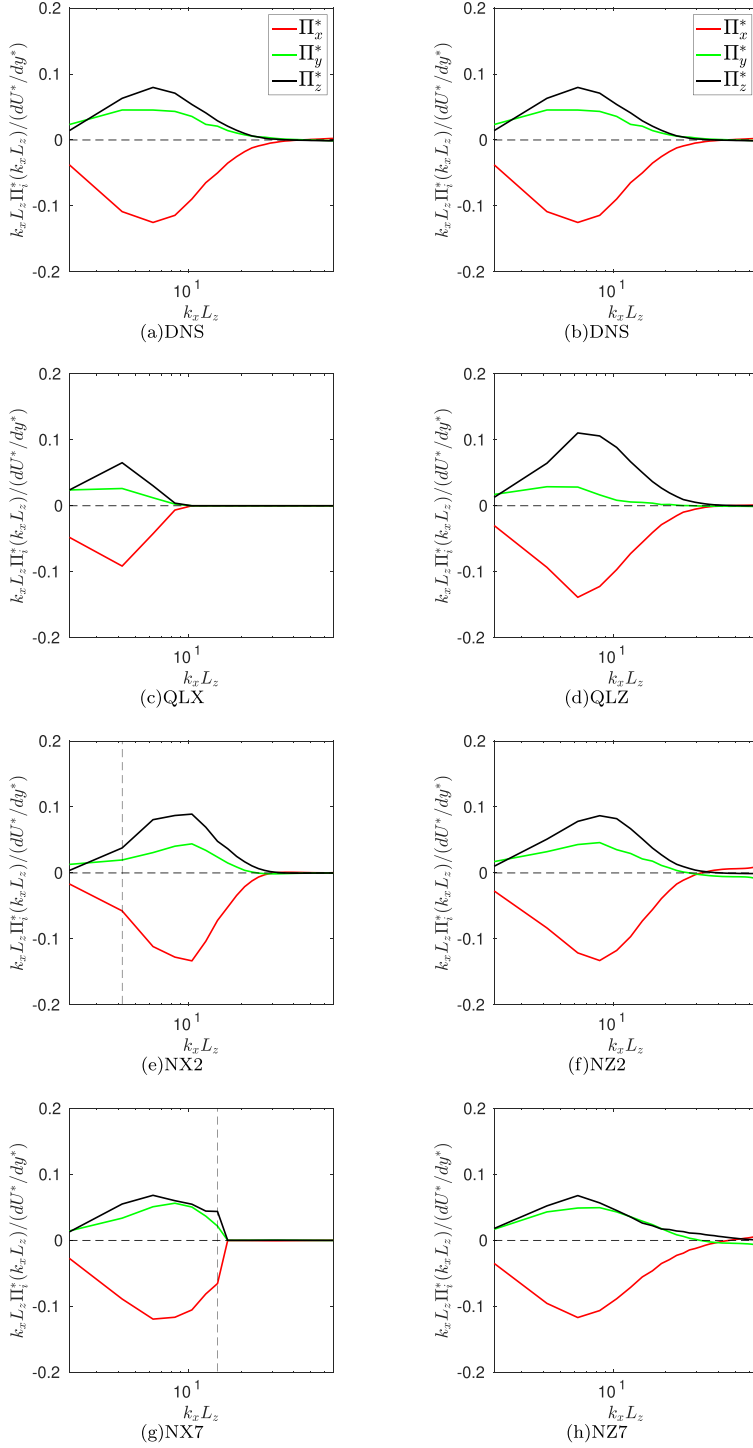
FIG. 9. Premultiplied streamwise wave-number spectra of the pressure-strain transport: (a, b) DNS; (c) QLX; (d) QLZ; (e) NX2; (f) NZ2; (g) NX7; (h) NZ7. The vertical lines represent the streamwise cutoff wave numbers ($k_{x,c}$) dividing the $\mathcal{P}_h$- (right) and $\mathcal{P}_l$-subspace (left) regions.

wall-bounded turbulence studied previously [29,30,34–36,54], the homogeneous shear turbulence contains a single (integral) length scale controlled by the spanwise computational domain, whose dynamics is well described by the so-called "self-sustaining process" [40,41]. This feature has been crucial in gaining the understanding of the precise roles of the GQL approximation in the self-sustaining process given at the single integral length scale (in particular, in the QL model the elongated streaks are captured by the streamwise mean and the streamwise undulating instability is captured by the linearized equations). The spectral energetics of the QL and GQL models have been analyzed and compared to that of DNS, with a focus on the study of streamwise and spanwise nonlinear energy transport. As expected, the QL approximation significantly inhibits the energy cascade in the direction along which it is applied, i.e., streamwise direction for QLX and spanwise direction for QLZ. The energy cascade is shown to be gradually recovered when more Fourier modes are incorporated in the $\mathcal{P}_l$ subspace. However, the implementation of the GQL approximation has revealed that there are some nontrivial points which deserve further discussions: (1) nonmonotonic convergence of the GQL model as more Fourier modes are incorporated into the $\mathcal{P}_l$-subspace group, and the dependence of the energy transfer to the $\mathcal{P}_h$ subspace on the cutoff wavelengths $\lambda_{r,c}$ and (2) similarities and differences between the GQL approximations made in the streamwise and spanwise directions (i.e., NX no. and NZ no. cases), with special attention to the maintenance of turbulence generated by the QL model in the spanwise direction (QLZ case). Here point (1) (i.e., the nonmonotonic convergence of the GQL model) was also observed in a recent PhD thesis that considered a set of GQL approximations for turbulent channel flow [60]. We will address these points in this section.

A. Nonmonotonic convergence and energy transfer to the high-wave-number group

In Sec. III it has been observed that the scattering mechanism in the GQL model [i.e., the energy transfer from $\mathcal{P}_l$ to $\mathcal{P}_h$ spaces through the second and third terms in Eq. (4b)] is not present when the cutoff wavelength $\lambda_{r,c}$ is sufficiently low: Figs. 3 and 4 show that the spectral intensity for $\lambda_r < \lambda_{r,c}$ ($r = x$ or z) in NX7, NZ4, NZ7, and N77 is zero, a result difficult to understand solely owning to the proposed scattering mechanism. As previously discussed in Ref. [35], this behavior originates from the linear nature of the equations for the $\mathcal{P}_h$-subspace group. The velocity component $\mathbf{u}_h$ is governed by the linear equation (4b) whose last two terms $\mathcal{P}_h[(\mathbf{u}_l \cdot \nabla)\mathbf{u}_l]$ and $\mathcal{P}_h[(\mathbf{u}_h \cdot \nabla)\mathbf{u}_h]$ are neglected by the GQL approximation. We note that the equation (4b) is linear and has no driving term, thereby written as follows:

$$\frac{\partial \mathbf{u}_h}{\partial t} = \mathcal{L}(\mathbf{U}_l)\mathbf{u}_h, \tag{21}$$

where $\mathcal{L}$ is an autonomous linear operator. For a QL/GQL model to be well posed (i.e., not blow up) with chaotic $\mathbf{U}_l$, the resulting stable solution should lead to $\mathbf{u}_h$ in the form of either the nontrivial neutrally stable leading Lyapunov vector (e.g., [20,54]) or the trivial solution (i.e., zero). Therefore, the leading Lyapunov exponent of the linear equations $\mathcal{L}(\mathbf{U}_l)$ should be either negative or zero for the QL/GQL model to not blow up: in other words, $\mathbf{u}_h$ can only decay or be marginally stable. In the particular case of the turbulent state produced by the QL/GQL approximation, the leading Lyapunov exponent from (21) must be zero [20,54], if Eq. (21) admits a nontrivial solution. Otherwise, the only possible solution is the trivial solution.

As $\lambda_{r,c}$ is decreased from a large value (or $M_{r,F}$ is increased), the smallest timescale of the velocity field $\mathbf{U}_l$ is expected to be reduced. This is because the decrease of $\lambda_{r,c}$ would admit $\mathbf{U}_l$ to contain more smaller length scales. Given that the leading Lyapunov exponent is inversely proportional or is even larger to the smallest timescale of the motion about which the equation is linearized (e.g., [61,62]), the decrease in $\lambda_{r,c}$ could lead the linearized equations for a given wave number in the $\mathcal{P}_h$ subspace to become more unstable before they reach the statistically stationary state. This is consistent with the spectra of the $\mathcal{P}_h$-subspace group shown in Figs. 3 and 4, which are extended to smaller wavelengths on decreasing $\lambda_{r,c}$. However, if $\lambda_{r,c}$ is too small, the linearized

equations may admit only the trivial solution in the $\mathcal{P}_h$ subspace due to the strong viscous damping effect, which explains why the spanwise wave-number spectra of NZ4, NZ7, and N77 cases (Fig. 3) and the streamwise wave-number spectra of the NX7 and N77 cases (Fig. 4) exhibit the trivial solution for $\lambda_r < \lambda_{r,c}$. This is a physical rationale explaining the nonmonotonic convergence of the GQL model: when the cutoff wavelength is too large, the high wave numbers are not excited by the scattering mechanism; however, if the cutoff wavelength is too small (e.g., near Kolmogorov length scale), the scattering mechanism is completely suppressed by the mechanism discussed above. This suggests that there exists a sweet spot in the choice of $\lambda_{r,c}$ for the performance of GQL, in which the scattering mechanism can excite sufficiently small length scales close to the Kolmogorov length scale. It appears that this is the best possible choice of cutoff wavelength, explaining why the NX7 case does not show better performance than NX2 or NX4; in fact, NX2 gives the closest statistics compared to DNS. A simple improvement of this behavior of the NX7 case within the quasilinear framework could be obtained by adding a forcing resembling the low-wave-number interaction terms in the $\mathcal{P}_h$-subspace group, whose contribution has recently been shown to become important when the scattering mechanism plays little role in generating the fluctuation in the $\mathcal{P}_h$ subspace (i.e., when the cutoff wavelength is sufficiently small) [36].

B. Comparison between QL/GQL approximations in the streamwise and spanwise directions

When the cutoff wavelength $\lambda_{r,c}$ is large, the QL/GQL models (with approximations taken along the streamwise or spanwise directions) have been shown to hold a common feature: they all exhibit a highly anisotropic turbulent fluctuation which contains significantly elevated energy in the streamwise component. This originates from the fact that, first, in parallel wall-bounded shear flows the turbulence production appears only in the streamwise component. Second, the pressure strain transfers the energy produced at the streamwise component to the other two components. Third, since the GQL approximations prevent the energy distribution mechanism into the other velocity components (through the damped slow pressure), it results in the overpredicted streamwise component of the velocity exhibited in the QL/GQL cases: for further discussions, see also [32,35,36].

There are, however, differences between the QL/GQL approximations made in the streamwise and spanwise directions (i.e., NX no. and NZ no. cases). First, the inhibition of the spectral energy transfer by the QL/GQL approximation appears to be more significant in the spanwise direction than in the streamwise direction. Indeed, the spectral energy budget spectra show that the QL/GQL approximations made in the spanwise direction tend to more sharply cut off the energy transfer from $\mathcal{P}_l$ to $\mathcal{P}_h$ subspaces than those made in the streamwise direction [in particular, compare Fig. 6(f) (NZ2) with Fig. 7(e) (NX2)], indicating that the scattering mechanism at least in the homogeneous shear flow is more effective in the streamwise direction. Second, the pressure strain spectra suggest that the QL/GQL approximations made in the streamwise direction are significantly less capable of transferring energy produced in the streamwise component to the other two components than those made in the spanwise direction. This is particularly apparent in the comparison between the pressure strain spectra of QLX and QLZ cases [see Figs. 8(c) and 8(d) and Figs. 9(c) and 9(d)], consistent with more anisotropic velocity fluctuations of the QLX case than those of the QLZ case reported in Table II. In fact, it is interesting to observe that the first- and second-order turbulence statistics from the QLZ case are equally good compared to those from the QLX case, if they are not seen better (see Table II). Having said this, the QLX case has often been referred to as a minimal model capturing the self-sustaining process [29–31]: $\mathbf{u}_l$ in the QLX case fully describes the nonlinear evolution of streaks, while the instability wave of the streaks is captured by the linearized equations for $\mathbf{u}_h$. Therefore, it is important to mention that the better turbulence statistics of the QLZ case do not necessarily imply that the QLZ case provides a dynamically more consistent description for turbulence in DNS than the QLX does and that the observation here may simply be a coincidence of the particular parameters used in the present study. However, the sustaining turbulence in the QLZ case does suggest that there might exist an uncovered mechanism that supports sustaining turbulence other than the self-sustaining process in shear flows [40,41]. At this point, at least the following four

scenarios might be possible to explain the sustaining mechanism of the QLZ case: (1) inflectional instability and/or the related transient growth of the spanwise mean flow caused by nontrivial dynamics of single streaky structures in the high-wave-number group; (2) inflectional instability and/or transient growth of the spanwise mean flow by interactions of vertically stacked multiple streaky structures (since our simulations involve multiple streaky motions in the y direction); (3) parametric instability associated with either of the dynamics proposed in (1) and (2); and (4) some other mechanisms that do not belong to all the scenarios mentioned. The simulations designed here would not allow us to separately examine each of these scenarios, requiring a further investigation on this issue. Therefore, it remains uncertain which of the mechanisms play a role in the self-sustaining turbulence in the QLZ case and whether it is more important than the self-sustaining process. These are the issues of our current investigation.

V. CONCLUSIONS

In the present study, the spectral energetics of the QL/GQL approximations applied to homogeneous shear turbulence is investigated and compared to that of DNS. For the QL/GQL approximations, the flow is decomposed into low- and high-streamwise-wave-number groups, the former of which is solved by considering the full nonlinear equations, whereas the latter is obtained from the linearized equations around the former. Given that the large-scale dynamics of the homogeneous shear turbulence is well described by the so-called "self-sustaining process" [40,41], this study provides a convenient framework to understand the energy cascade and turbulent dissipation associated with the self-sustaining process. Unlike the QL model, which shows an active cascade in one direction and a disruption of it in the other direction because of the linearization in the given approximation, the GQL model shows healthier energy cascades along the direction in which more Fourier modes are included in the $\mathcal{P}_l$ subspace (e.g., spanwise energy cascade of NZ2 case), resulting in a better description of the dynamics and statistics of the given flow than the QL model. As in the previous study [32], the slow pressure is commonly damaged by this type of approximations made in any directions, yielding an overprediction of the streamwise component of the velocity due to the lack of componentwise energy distribution mechanism mediated by the related pressure strain. Nonmonotonic convergence of turbulence statistics of the QL/GQL approximation to those of DNS is also discussed in relation to the scattering mechanism (e.g., [34]) and the neutral Lyapunov vector being the nontrivial solution to the equations for the $\mathcal{P}_h$ subspace (e.g., [25]). Finally, the QL/GQL models applied to the streamwise and spanwise directions are compared.

[1] G. K. Batchelor and I. Proudman, The effect of rapid distortion of a fluid in turbulent motion, Q. J. Mech. Appl. Math. **7**, 83 (1954).

[2] J. C. R. Hunt and D. J. Carruthers, Rapid distortion theory and the problems of turbulence, J. Fluid Mech. **212**, 497 (1990).

[3] L. N. Trefethen, A. E. Trefethen, S. C. Reddy, and T. A. Driscoll, Hydrodynamic stability without eigenvalues, Science **261**, 578 (1993).

[4] K. M. Butler and B. F. Farrell, Optimal perturbations and streak spacing in wall-bounded turbulent shear flow, Phys. Fluids A: Fluid Dyn. **5**, 774 (1993).

[5] B. F. Farrell and P. J. Ioannou, Optimal excitation of three-dimensional perturbations in viscous constant shear flow, Phys. Fluids A: Fluid Dyn. **5**, 1390 (1993).

[6] S. C. Reddy and D. S. Henningson, Energy growth in viscous channel flows, J. Fluid Mech. **252**, 209 (1993).

[7] P. J. Schmid and D. S. Henningson, Optimal energy density growth in Hagen-Poiseuille flow, J. Fluid Mech. **277**, 197 (1994).

[8] B. Bamieh and M. Dahleh, Energy amplification in channel flows with stochastic excitation, Phys. Fluids **13**, 3258 (2001).

[9] M. R. Jovanović and B. Bamieh, Componentwise energy amplification in channel flows, J. Fluid Mech. **534**, 145 (2005).

[10] J. Kim and J. Lim, A linear process in wall-bounded turbulent shear flows, Phys. Fluids **12**, 1885 (2000).

[11] J. C. Del Alamo and J. Jimenez, Linear energy amplification in turbulent channels, J. Fluid Mech. **559**, 205 (2006).

[12] C. Cossu, G. Pujals, and S. Depardon, Optimal transient growth and very large–scale structures in turbulent boundary layers, J. Fluid Mech. **619**, 79 (2009).

[13] Y. Hwang and C. Cossu, Linear non-normal energy amplification of harmonic and stochastic forcing in turbulent channel flow, J. Fluid Mech. **664**, 51 (2010).

[14] B. J. McKeon and A. S. Sharma, A critical-layer framework for turbulent pipe flow, J. Fluid Mech. **658**, 336 (2010).

[15] A. Zare, M. R. Jovanović, and T. T. Georgiou, Colour of turbulence, J. Fluid Mech. **812**, 636 (2017).

[16] J. R. Herring, Investigation of problems in thermal convection, J. Atmos. Sci. **20**, 325 (1963).

[17] W. V. R. Malkus, The heat transport and spectrum of thermal turbulence, Phil. Trans. R. Soc. A **225**, 196 (1954).

[18] W. V. R. Malkus, Outline of a theory of turbulent shear flow, J. Fluid Mech. **1**, 521 (1956).

[19] B. F. Farrell and P. J. Ioannou, Structure and spacing of jets in barotropic turbulence, J. Atmos. Sci. **64**, 3652 (2007).

[20] B. F. Farrell and P. J. Ioannou, Dynamics of streamwise rolls and streaks in turbulent wall-bounded shear flow, J. Fluid Mech. **708**, 149 (2012).

[21] J. B. Marston, E. Conover, and T. Schneider, Statistics of an unstable barotropic jet from a cumulant expansion, J. Atmos. Sci. **65**, 1955 (2008).

[22] S. M. Tobias and J. B. Marston, Direct Statistical Simulation of Out-of-Equilibrium Jets, Phys. Rev. Lett. **110**, 104502 (2013).

[23] V. Mantič-Lugo, C. Arratia, and F. Gallaire, Self-Consistent Mean Flow Description of the Nonlinear Saturation of the Vortex Shedding in the Cylinder Wake, Phys. Rev. Lett. **113**, 084501 (2014).

[24] V. Mantič-Lugo and F. Gallaire, Saturation of the response to stochastic forcing in two-dimensional backward-facing step flow: A self-consistent approximation, Phys. Rev. Fluids **1**, 083602 (2016).

[25] B. F. Farrell, D. F. Gayme, and P. J. Ioannou, A statistical state dynamics approach to wall turbulence, Philos. Trans. R. Soc. A **375**, 20160081 (2017).

[26] D. F. Gayme and B. A. Minnick, Coherent structure-based approach to modeling wall turbulence, Phys. Rev. Fluids **4**, 110505 (2019).

[27] B. A. Minnick and D. F. Gayme, Characterizing energy transfer in restricted nonlinear wall-bounded, in *11th Intl. Symp. on Turbulence and Shear Flow Phenomena, Southampton, United Kingdom* (2019), p. 145.

[28] J. U. Bretheim, C. Meneveau, and D. F. Gayme, Standard logarithmic mean velocity distribution in a band-limited restricted nonlinear model of turbulent flow in a half-channel, Phys. Fluids **27**, 011702 (2015).

[29] V. L. Thomas, B. F. Farrell, P. J. Ioannou, and D. F. Gayme, A minimal model of self-sustaining turbulence, Phys. Fluids **27**, 105104 (2015).

[30] V. L. Thomas, B. K. Lieu, M. R. Jovanović, B. F. Farrell, P. J. Ioannou, and D. F. Gayme, Self-sustaining turbulence in a restricted nonlinear model of plane Couette flow, Phys. Fluids **26**, 105112 (2014).

[31] M. Pausch, Q. Yang, Y. Hwang, and B. Eckhardt, Quasilinear approximation for exact coherent states in parallel shear flows, Fluid Dyn. Res. **51**, 011402 (2019).

[32] C. G. Hernández and Y. Hwang, Spectral energetics of a quasilinear approximation in uniform shear turbulence, J. Fluid Mech. **904**, A11 (2020).

[33] J. B. Marston, G. P. Chini, and S. M. Tobias, Generalized Quasilinear Approximation: Application to Zonal Jets, Phys. Rev. Lett. **116**, 214501 (2016).

[34] S. M. Tobias and J. B. Marston, Three-dimensional rotating Couette flow via the generalised quasilinear approximation, J. Fluid Mech. **810**, 412 (2017).

[35] C. G. Hernández, Q. Yang, and Y. Hwang, Generalised quasilinear approximations of turbulent channel flow. Part 1. Streamwise nonlinear energy transfer, J. Fluid Mech. **936**, A33 (2022).

[36] C. G. Hernández, Q. Yang, and Y. Hwang, Generalised quasilinear approximations of turbulent channel flow: Part 2. Spanwise triadic scale interactions, J. Fluid Mech. **944**, A34 (2022).

[37] Y. Hwang and B. Eckhardt, Attached eddy model revisited using a minimal quasi-linear approximation, J. Fluid Mech. A **894**, 23 (2020).

[38] N. Skouloudis and Y. Hwang, Scaling of turbulence intensities up to $_\tau = 10^6$ with a resolvent-based quasilinear approximation, Phys. Rev. Fluids **6**, 034602 (2021).

[39] G. Michel and G. P. Chini, Multiple scales analysis of slow-fast quasi-linear systems, Proc. R. Soc. A: Math. Phys. Eng. Sci. **475**, 20180630 (2019).

[40] J. M. Hamilton, J. Kim, and F. Waleffe, Regeneration mechanisms of near-wall turbulence structures, J. Fluid Mech. **287**, 317 (1995).

[41] F. Waleffe, On a self-sustaining process in shear flows, Phys. Fluids **9**, 883 (1997).

[42] A. Sekimoto, S. Dong, and J. Jiménez, Direct numerical simulation of statistically stationary and homogeneous shear turbulence and its relation to other shear flows, Phys. Fluids **28**, 035101 (2016).

[43] Q. Yang, A. P. Willis, and Y. Hwang, Energy production and self-sustained turbulence at the Kolmogorov scale in Couette flow, J. Fluid Mech. **834**, 531 (2018).

[44] N. A. Bakas and P. J. Ioannou, Emergence of Large Scale Structure in Barotropic β-Plane Turbulence, Phys. Rev. Lett. **110**, 224501(2013).

[45] N. A. Bakas and P. J. Ioannou, A theory for the emergence of coherent structures in beta-plane turbulence, J. Fluid Mech. **740**, 312 (2014).

[46] N. A. Bakas, N. C. Constantinou, and P. J. Ioannou, S3t stability of the homogeneous state of barotropic beta-plane turbulence, J. Atmos. Sci. **72**, 1689 (2015).

[47] N. C. Constantinou, Formation of large-scale structures by turbulence in rotating planets, Ph.D. thesis, National and Kapodistrian University of Athens, Athens, 2015.

[48] N. C. Constantinou, B. F. Farrell, and P. J. Ioannou, Statistical state dynamics of jet–wave coexistence in barotropic beta-plane turbulence, J. Atmos. Sci. **73**, 2229 (2016).

[49] U. Frisch, *Turbulence: The Legacy of A. N. Kolmogorov* (Cambridge University Press, Cambridge, 1995).

[50] M. Cho, Y. Hwang, and H. Choi, Scale interactions and spectral energy transfer in turbulent channel flow, J. Fluid Mech. **854**, 474 (2018).

[51] T. Bewley, *Numerical Renaissance: Simulation, Optimisation and Control* (Renaissance Press, 2014).

[52] P. Doohan, A. P. Willis, and Y. Hwang, Shear stress-driven flow: The state space of near-wall turbulence $_\tau \to \infty$, J. Fluid Mech. **874**, 606 (2019).

[53] J. Kim and P. Moin, Application of a fractional-step method to incompressible Navier-Stokes equations, J. Comput. Phys. **59**, 308 (1985).

[54] B. F. Farrell, P. J. Ioannou, J. Jiménez, N. C. Constantinou, A. Lozano-Durán, and M.-A. Nikolaidis, A statistical state dynamics-based study of the structure and mechanism of large-scale motions in plane Poiseuille flow, J. Fluid Mech. **809**, 290 (2016).

[55] W. Schoppa and F. Hussain, Coherent structure generation in near-wall turbulence, J. Fluid Mech. **453**, 57 (2002).

[56] Y. Hwang and Y. Bengana, Self-sustaining process of minimal attached eddies in turbulent channel flow, J. Fluid Mech. **795**, 708 (2016).

[57] H. J. Bae, A. Lozano-Durán, and B. J. McKeon, Nonlinear mechanism of the self-sustaining process in the buffer and logarithmic layer of wall-bounded flows, J. Fluid Mech. **914**, A3 (2021).

[58] A. A. R. Townsend, *The Structure of Turbulent Shear Flow* (Cambridge University Press, Cambridge, 1976).

[59] J. Kim, On the structure of pressure fluctuations in simulated turbulent channel flow, J. Fluid Mech. **205**, 421 (1989).

[60] C. B. Kellam, Generalized quasilinear simulation of turbulent channel flow, Ph.D. thesis, University of New Hampshire, 2019.

[61] D. Ruelle, Microscopic fluctuations and turbulence, Phys. Lett. A **72**, 81 (1979).

[62] A. Crisanti, M. H. Jensen, G. Paladin, and A. Vulpiani, Predictability of velocity and temperature fields in intermittent turbulence, J. Phys. A: Math. Gen. **26**, 6943 (1993).